https://doi.org/10.1016/j.etran.2020.100074

Dynamic modeling and operation strategy of natural gas fueled SOFC-Engine hybrid power system with hydrogen addition by metal hydride for vehicle applications

Zhen Wu[1,2], Pengfei Zhu[1], Jing Yao[1], Peng Tan[3], Haoran Xu[2], Bin Chen[2], Fusheng Yang[1], Zaoxiao Zhang[1,4,*], Ekambaram Porpatham[5], Meng Ni[2,*]

[1]Shaanxi Key Laboratory of Energy Chemical Process Intensification, School of Chemical Engineering and Technology, Xi'an Jiaotong University, Xi'an, China

[2]Building Energy Research Group, Department of Building and Real Estate, The Hong Kong Polytechnic University, Hong Kong, China

[3]Department of Thermal Science and Energy Engineering, University of Science and Technology of China, Hefei 230026, Anhui, China

[4]State Key Laboratory of Multiphase Flow in Power Engineering, Xi'an Jiaotong University, Xi'an, China

[5]Automotive Research Centre, School of Mechanical Engineering, Vellore Institute of Technology, Vellore, India

*Corresponding author, Email: meng.ni@polyu.edu.hk (M Ni)

zhangzx@xjtu.edu.cn (Z Zhang)

Abstract: SOFC-Engine hybrid power system is a promising energy conversion technology with high efficiency. However, its dynamic behaviors are still unclear. Herein, the dynamic modeling of this hybrid system is performed. Besides, the control strategies of hydrogen addition and power distribution are further investigated to enhance the system performance. The results show that the relatively slow dynamics of the SOFC component is dominating in the hybrid system. The reason is mainly attributed to that the autonomy of the engine with fast dynamics is partly restricted without hydrogen addition. When hydrogen is fed to the engine as a part of inlet fuel by metal hydride and waste heat recovery unit, the dynamics of the hybrid system can be improved. Moreover, the efficiency can also be improved to 67.6% with the hydrogen addition ratio χ=2.0. After that, the control strategy for power distribution is proposed to achieve the optimal overall performance for the hybrid system. The SOFC provides most of the output power as a stable power baseline and the engine copes with the dynamic part. In such a strategy, the hybrid system enables to respond to the change of power load within 1 s and to achieve the overall energy conversion efficiency up to 75%, which is promising for the vehicle applications. In brief, this work can provide an insight into the dynamic behaviors of the SOFC-Engine hybrid energy conversion system to obtain the feasible operation strategy for its vehicle applications.

Keywords: Fuel cell; Engine; Hybrid power system; Dynamic modeling; Metal hydride

Nomenclature

Abbreviation

DC/AC	Direct current to alternating current
DIR	Direct internal reforming
FC	Fuel cell
GT	Gas turbine
HCCI	Homogeneous charge compression ignition
HE	Heat exchanger
HyT	Hydrogen tank
LHV	Lower heating value
MHR	Metal hydride reactor
MSR	Methane steam reforming
NG	Natural gas
SOFC	Solid oxide fuel cell
WGS	Water gas shift

Symbols

A	fuel cell area, m^2
C_d	hydrogen desorption reaction rate constant, 1/s
C_p	specific heat capacity, J/(kg K)
$\overline{C_p}$	average specific heat capacity, J/(kg K)
D^eff	effective diffusion coefficient, m/s
E_act	activation energy, J/mol
F	Faraday constant, C/mol
h	specific enthalpy, J/mol
I	current, A
J	current density, A/m^2
K	reaction equilibrium constant
k	reaction rate constant
l	thickness, m
$\dot{m}_{\mathrm{H}_2}$	hydrogen molar mass, mol/s
P	power, kW
p	pressure, bar
Q	heat, kW
r	reaction rate, mol/s
R	resistance, Ω
R_g	universal gas constant, J/(K mol)
t	time, s

T	temperature, K
V	cell voltage, V

Greek

χ_{O_2}	oxygen percent in the fuel
ϕ	mass or molar flow, kg/s or mol/s
τ	time constant, s
η	energy efficiency
γ	compression ratio
φ	equivalent ratio
ρ	density, kg/m^3
χ	H_2 addition

Subscript

a	anode
act	activation
as	ash
c	cathode
conc	concentration
comb	combustion
comp	compressor
CDL	charge double layer
e	electrolyte
eq	equilibrium

ex	expansion
exh	exhaust gas
ex-ref	external reforming
fu	fuel gas
ign	ignition
in	inlet
ISC	isentropy of compressor
IST	isentropy of turbine
MEC	mechanical efficiency of compressor
MET	mechanical efficiency of turbine
ohm	ohmic polarization
ox	oxidant
out	outlet
reform	reforming
turb	turbine

1. Introduction

An efficient and clean energy conversion and utilization way is crucial for sustainable development of human society. So far, traditional fossil fuels including coal, petroleum, and natural gas (NG), are still the main energy sources for human beings [1,2]. In such a context, how to use the NG fuel more efficiently and cleanly is always attracting attention in the energy field. The technology of internal combustion (IC) engines using compressed NG as the fuel to generate power is viewed as a clean energy conversion pathway for vehicles. However, its energy conversion efficiency is always less than 40% due to the thermodynamic limitation, mechanical loss and thermal loss [3,4]. Thus, innovative technologies for improving the energy conversion efficiency of the NG-fueled IC engine are in urgent demand.

As an innovative power generation technology, fuel cell (FC) has become one of the most promising power sources due to its high electrical efficiency and no emission of pollutants [5]. Considering these merits, FC presents a good potential to replace the IC engine [6,7]. As the electricity is generated by the electrochemical reaction of hydrogen and oxygen rather than a combustion process, the energy conversion efficiency is not limited by the Carnot thermodynamic cycle [8]. Solid oxide fuel cell (SOFC) usually operates at high temperatures of more than 873 K, which enables the use of various hydrocarbon fuels, such as NG, biogas, petroleum gas, and methane through high-temperature reforming and water gas shift (WGS) reactions [9]. Accordingly, a mass of heat is released along with the exhaust gas at such high temperatures, which can be reused by a waste heat recovery unit to drive bottoming thermodynamic cycles (e.g., Rankine, Brayton, and Otto cycles) for additional power generation [10–12]. Although the external combustion engine (such as Stirling engine) can also utilize the waste heat of the SOFC to drive the piston for power stroke to generate additional power [13,14], the effective power is low in practice, resulting in the low power density. In contrast to the external combustion engine utilizing waste heat, the IC engine can additionally utilize the combustible compositions (H_2, CO and hydrocarbon) of unconsumed fuel from the SOFC off-gas for additional power generation. It is confirmed that the heating value of the off-gas produced from the SOFC are higher than the generated waste heat from the electrochemical reactions [15]. On the other hand, the external combustion engine usually requires some auxiliary devices such as boiler and condenser, which significantly increases the system size and complexity. For the above reasons, the IC engine is introduced to integrate with the SOFC for utilizing both the SOFC waste heat and unconsumed fuel, which not only improves the overall energy conversion efficiency but also extends the power range to facilitate the practical applications.

More research has focused on the novel SOFC-IC engine hybrid system recently. Kang and Ahn [16] developed a dynamic model of an SOFC-engine hybrid system to evaluate dynamic behaviors. The report lays out a theoretical foundation for the operating strategies of the SOFC-engine hybrid system under different transient conditions. Lee et al. [17] evaluated an SOFC-Engine hybrid power generation system by using exergetic and exergoeconomic analysis methods. The results showed that the largest exergy destruction takes place within the IC engine and the highest exergoeconomic factor of 93% is observed in the SOFC stack. Chuahy et al. [18] adopted the method of computational system optimization to explore the efficiency potential of an electrochemical combustion combined system for distributed power generation. They concluded that the system is capable of achieving electrical efficiency over 70%. Oh et al. [19] investigated the feasibility of reducing the exergy destruction in the reforming process of a fuel cell system by using an HCCI engine as a replacement of existing reforming subsystems. The simulation results showed that the HCCI-SOFC system had the highest exergy efficiency compared to other reforming subsystems. Choi et al. [20] experimentally confirmed the feasibility of an SOFC-IC engine hybrid system by using the SOFC anode off-gas as the engine fuel. The burning anode off-gas in the engine could generate power with the efficiency of 25%~30% in a very low NO_x emission. Besides, the SOFC-IC engine hybrid system could achieve the overall energy conversion efficiency of 59.5% and the levelized cost of electricity (LCOE) was $0.23/kWh, both of which were better than the standalone SOFC and SOFC-GT hybrid systems [21]. They further investigated the SOFC operation and the design point of system operation for the SOFC-Engine hybrid system [22]. The SOFC component was suggested to utilize anode inlet gas with a low external reforming rate (30%~40%) and temperature (750~800 K). In a 5-kW SOFC-IC engine hybrid system [23], the exergy efficiency of about 37% and the efficiency of about 62% are achieved using a spark-assisted ignition for the IC engine. However, an additional heater instead of a waste heat recovery unit was installed to heat the external reformer in their studies. Meanwhile, the output power and energy conversion efficiency of the IC engine were a little small due to the lean combustion in the engine. To further improve the power and the efficiency, coupling a metal hydride reactor (MHR) for H_2 addition by a waste heat recovery unit was introduced into the SOFC-IC engine hybrid system in our previous study [24]. The overall efficiency was found to be increased to 79.54% by H_2 addition from the MHR for the IC engine and H_2 recirculation for the SOFC anode off-gas suggesting that the SOFC-Engine hybrid system is a promising energy conversion system. The fuel flexibility and extended output power demonstrate the potential of the hybrid SOFC-IC engine system for vehicle applications, especially the heavy bus, truck and marine ship. Since the dynamic behaviors of the power generation system are important for vehicles in practical, the two different power generation components have different transient responses and interact with each other. Thus, it is essential to investigate the dynamic behaviors of the proposed SOFC-Engine hybrid system for achieving the optimal operation and control strategies for vehicles. However, to our knowledge, no works have been reported on the dynamic modeling and operation strategy of the hybrid system yet.

In the present study, the dynamic modeling of the novel NG fueled SOFC-Engine hybrid energy conversion system is conducted. Then, the dynamic behaviors of the hybrid system are investigated under different operating conditions. The composition structure of this paper is set as follow: In Section 2, the system description and working principle are introduced. The system modeling including the thermodynamics model of the key components is also presented. Then the computational details are given and model validation is conducted. In Section 3, the system dynamic performance is evaluated firstly. Then the overall energy conversion efficiency of the hybrid system at different H_2 addition ratios is investigated. The dynamic characteristic of the hybrid system with different H_2 addition ratios and addition modes is further analyzed. Finally, the power distribution and control strategy in different SOFC fuel utilization and power ratios are discussed in detail. In short, this work can provide an insight into the dynamic behaviors of the SOFC-Engine hybrid energy conversion system to obtain the feasible operation strategy for its practical applications such as ships and heavy truck.

2. System modeling

2.1. System description

The proposed SOFC-Engine hybrid system is mainly comprised of the SOFC and IC engine subsystems, as illustrated in Fig. 1. In the SOFC subsystem, the fuel source NG (CH_4: 85%, C_2H_6: 7%, C_3H_8: 2%, CO_2: 5%, N_2: 1%) passes through the external reformer in the first place and is partially converted into CO and H_2. The outlet gas (CH_4: 27.75%, C_2H_6: 2.28%, C_3H_8: 0.65%, CO_2: 11.49%, N_2: 0.54%, CO: 10.27%, H_2: 26.77%, H_2O: 20.25%) of the external reformer is first preheated by the SOFC anode off-gas using a heat exchanger and then injected into the SOFC as fuel for power generation. Similarly, the air is also first preheated to the same temperature by the cathode off-gas before entering the SOFC cathode. For the main component SOFC, the transient responses of electrochemistry and fuel processor are modeled to predict the dynamic behaviors of SOFC. In the

IC engine subsystem, the SOFC off-gas enters the downstream engine as the fuel and goes through the processes of compression, combustion, expansion and exhaust strokes in sequence for additional power generation. Since the SOFC off-gas is a lean fuel (a few combustible constituents), the combustion method of homogeneous charge compression ignition (HCCI) [25] is chosen for the engine to preferably burn the lean fuel. To improve the thermal efficiency, the waste heat of the exhaust gas of the HCCI engine is recycled to heat the fuel source and water from room temperature to the ex-reforming temperature and also serve as heat sources for the ex-reforming reaction and H_2 desorption reaction of MHR. As the engine operating speed is generally more than 1500 rpm [26], the time scale for the engine reaction is much shorter than that for the SOFC. Therefore, only the auto-ignition modeling is considered for the engine without the dynamics of intake fuel gas and combustion reaction.

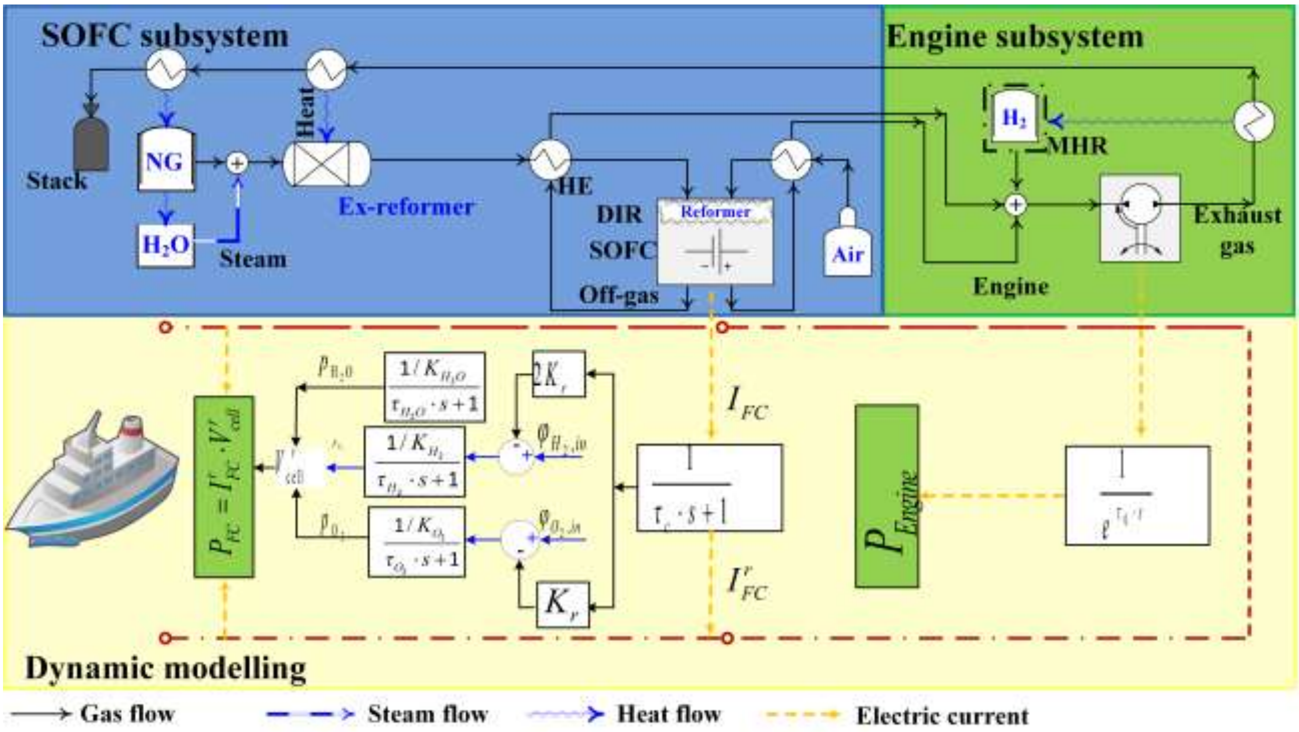

Fig. 1. Schematic diagram of the SOFC-Engine hybrid power system with H_2 addition for vehicles

2.2. System modeling

To simplify the system model, the following assumptions are employed.

1) All gases are approximated as ideal gases.

2) The system is completely insulated. No heat transfer takes place between the system and the environment [27,28].
3) Pressure drops in the system are neglected because of the small pressure loss for the main SOFC and engine as the main components [29–31]. The pressure drops of the main components SOFC, heat exchanger and compressor were reported to be lower than 5% even in the pressurized SOFC-engine hybrid system [32].
4) No carbon deposition occurs due to the high ratio of steam to carbon S/C [33].
5) The internal reforming and electrochemical reactions are separately modeled in the SOFC. Although the reformed gas component CO can be also consumed by an electrochemical reaction, the WGS reaction converting CO into H_2 always preferentially occurs in the presence of H_2O. Thus, only H_2 participates in the electrochemical reaction inside the SOFC.
6) Since the time required for temperature changes in SOFC is much longer than the time scale of electrochemical dynamics and fuel processing, the dynamic effects of temperature changes in SOFC can be ignored in such a short scale time (the response time of electrochemistry and fuel processor) [34]. Hence, the temperature of the fuel cell is assumed to be stable in this dynamic simulation.
7) The reforming and WGS reactions are assumed to be in equilibrium due to the rather fast H_2 production rates (~3500 $mol/s/kg_{cat}$ at 823 K and ~1.8×10^{7} $mol/s/kg_{cat}$ at 1073 K). Since this work focuses on dynamic modeling and operational strategy for SOFC-Engine hybrid systems, the spatial distribution and structure of catalysts are not been fully considered. Fig. 2 shows the effects of ignoring the reforming dynamics on the SOFC power and H_2 production variations under the conditions of 823 K and 101.3 kPa. No remarkable effect appears in the SOFC power due to slow FC response time (>1 s time scale) even though H_2 production changes in the initial few seconds.

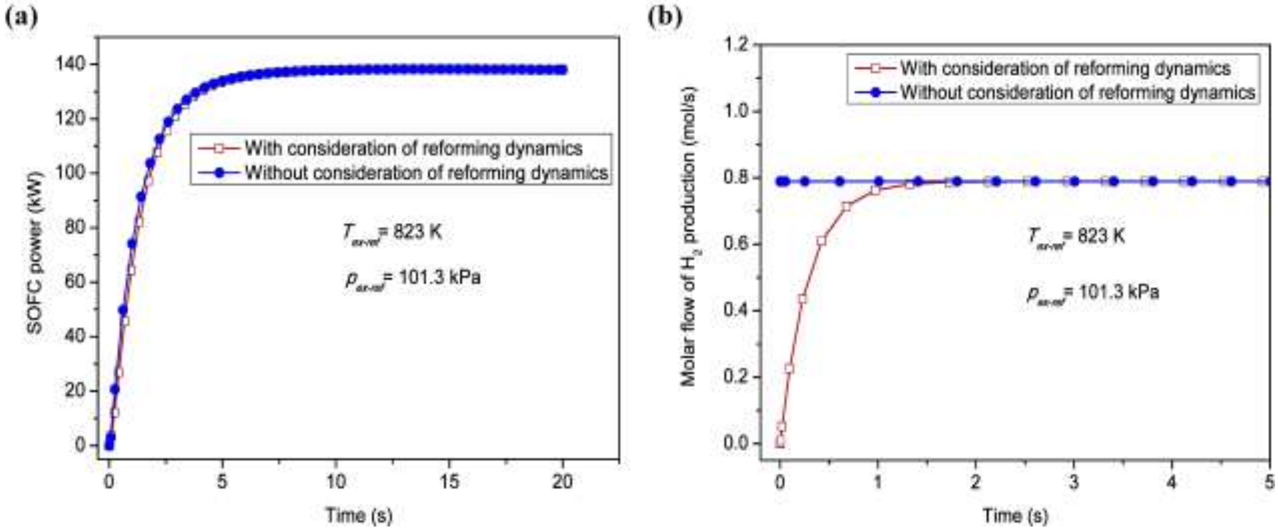

Fig. 2. The effects of ignoring the dynamics of reforming reactions on SOFC performance. (a) SOFC power; (b) H_2 production.

8) The hysteresis effect between the hydrogen absorption and desorption process is neglected due to the small hysteresis factor $\ln(p_{eq,a}/p_{eq,d})=0.13$ [35].

2.2.1 SOFC electrochemical modeling

The electrochemical reaction between H_2 and O_2 occurring in the SOFC can be expressed in Eq. (1). It should be noticed that only H_2 is assumed as the fuel for electrochemical oxidation in the SOFC anode. Although CO can also be electrochemically oxidized in the anode, its reaction rate is lower than that of the H_2 fuel. Moreover, the WGS reaction converting CO into H_2 always preferentially occurs in the presence of water.

$$\mathrm{H_2} + \frac{1}{2}\mathrm{O_2} \rightarrow \mathrm{H_2O(g)} \quad \Delta H = \text{-242 kJ / mol} \tag{1}$$

Eqs. (2-3) show the SOFC electrochemical model, which describes the relationship between cell voltage V_{cell} and irreversible overvoltage [36,37]. E_{N} is the thermodynamic potential of the fuel cell. Generally, three kinds of irreversible overvoltage are considered, including the activation overvoltage V_{act}, ohmic overvoltage V_{ohm}, and concentration overvoltage V_{conc}.

$$V_{\mathrm{cell}} = E_{\mathrm{N}} - V_{\mathrm{act}} - V_{\mathrm{ohm}} - V_{\mathrm{conc}} \tag{2}$$

$$E_{\mathrm{N}} = 1.253 - 2.4516\times10^{-4}\cdot T_{\mathrm{SOFC}} - \frac{R_{\mathrm{g}}\cdot T_{\mathrm{SOFC}}}{4F}\cdot\ln\left(\frac{p_{\mathrm{H_2O}}^2}{p_{\mathrm{H_2}}^2\cdot p_{\mathrm{O_2}}}\right) \tag{3}$$

where T_{SOFC} is the SOFC temperature; R_{g} is the ideal gas constant; F is the Faraday constant (96485 C/mol); $p_{\mathrm{H_2}}$, $p_{\mathrm{O_2}}$, and $p_{\mathrm{H_2O}}$ stand for the partial pressure of H_2, O_2, and water vapor, respectively.

The activation overvoltage V_{act} is caused by the necessary activation of charge transfer for electrodes, which is determined by the Butler-Volmer equation. The SOFC activation overvoltage is given by Eq. (4), among which the exchange current density J_0 is related to the electrode microstructure and the operating conditions [38]. The corresponding anode and cathode exchange current density $J_{0,\mathrm{a}}$ and $J_{0,\mathrm{c}}$ can be calculated by $J_{0,\mathrm{a}} = 1.3448\times10^{10} \cdot \left(\frac{p_{\mathrm{H_2}}}{p_{\mathrm{ref}}}\right) \cdot \left(\frac{p_{\mathrm{H_2O}}}{p_{\mathrm{ref}}}\right) \cdot e^{-\frac{E_{\mathrm{act,a}}}{R_{\mathrm{g}} \cdot T_{\mathrm{SOFC}}}}$ and $J_{0,\mathrm{c}} = 2.051\times10^{9} \cdot \left(\frac{p_{\mathrm{O_2}}}{p_{\mathrm{ref}}}\right)^{0.25} \cdot e^{-\frac{E_{\mathrm{act,c}}}{R_{\mathrm{g}} \cdot T_{\mathrm{SOFC}}}}$ [38].

$$\begin{aligned} V_{\mathrm{act}} &= V_{\mathrm{act,a}} + V_{\mathrm{act,c}} \\ &= \frac{R_{\mathrm{g}} \cdot T_{\mathrm{SOFC}}}{F} \cdot \ln\left[\frac{J}{2J_{0,\mathrm{a}}} + \sqrt{\left(\frac{J}{2J_{0,\mathrm{a}}}\right)^2 + 1}\right] + \frac{R_{\mathrm{g}} \cdot T_{\mathrm{SOFC}}}{F} \cdot \ln\left[\frac{J}{2J_{0,\mathrm{c}}} + \sqrt{\left(\frac{J}{2J_{0,\mathrm{c}}}\right)^2 + 1}\right] \end{aligned} \tag{4}$$

where J is the current density; $E_{\mathrm{act,a}}$ and $E_{\mathrm{act,c}}$ represent the activation energy of anode and cathode electrode, respectively.

The ohmic overvoltage $V_{\mathrm{ohm}} = I \cdot R_{\mathrm{ohm}}$ is caused by the ohmic resistance R_{ohm}. Generally, the resistance to the oxygen ion transfer through the electrolyte mainly contributes to R_{ohm} for the SOFC. Generally, V_{ohm} can be simplified in the following equation [38].

$$V_{\mathrm{ohm}} = 2.99\times10^{-11} \cdot J \cdot l_{\mathrm{e}} \cdot e^{\frac{10300}{T_{\mathrm{SOFC}}}} \tag{5}$$

where l_{e} is the electrolyte thickness.

The concentration overvoltage V_{conc} of the SOFC is given in Eq. (6) [38]. It should be noted that the concentration overvoltage is ignored at the low current density region to avoid the non-convergence of the dynamic modeling. This treatment is valid as the gas transport is not a limiting factor at a low current density.

$$\begin{aligned} V_{\mathrm{conc}} &= V_{\mathrm{conc,a}} + V_{\mathrm{conc,c}} \\ &= \frac{R \cdot T_{\mathrm{SOFC}}}{2F} \cdot \ln\left(\frac{1 + \dfrac{R_{\mathrm{g}} \cdot T_{\mathrm{SOFC}} \cdot l_{\mathrm{a}} \cdot J}{2F \cdot D_{\mathrm{a}}^{\mathrm{eff}} \cdot p_{\mathrm{H_2O}}}}{1 - \dfrac{R_{\mathrm{g}} \cdot T_{\mathrm{SOFC}} \cdot l_{\mathrm{a}} \cdot J}{2F \cdot D_{\mathrm{a}}^{\mathrm{eff}} \cdot p_{\mathrm{H_2}}}} \right) + \frac{R \cdot T_{\mathrm{SOFC}}}{4F} \cdot \ln\left(\frac{p_{\mathrm{O_2}}}{\dfrac{p_{\mathrm{c}}}{\delta_{\mathrm{O_2}}} - \left(\dfrac{p_{\mathrm{c}}}{\delta_{\mathrm{O_2}}} - p_{\mathrm{O_2}} \right) \cdot e^{\frac{R_{\mathrm{g}} \cdot T_{\mathrm{SOFC}} \cdot l_{\mathrm{c}} \cdot J \cdot \delta_{\mathrm{O_2}}}{4F \cdot D_{\mathrm{c}}^{\mathrm{eff}} \cdot p_{\mathrm{c}}}}} \right) \end{aligned} \tag{6}$$

where l_{a} and l_{c} stand for the anode and cathode thickness, respectively; $D_{\mathrm{a}}^{\mathrm{eff}}$ and $D_{\mathrm{c}}^{\mathrm{eff}}$ are the effective diffusion coefficients of anode and cathode, respectively, which are $D_{\mathrm{a}}^{\mathrm{eff}} = \frac{\varepsilon}{\theta} \cdot \frac{D_{\mathrm{H_2\text{-}H_2O}} \cdot D_{\mathrm{H_2,k}}}{D_{\mathrm{H_2\text{-}H_2O}} + D_{\mathrm{H_2,k}}}$ for the anode and $D_{\mathrm{c}}^{\mathrm{eff}} = \frac{\varepsilon}{\theta} \cdot \frac{D_{\mathrm{O_2\text{-}N_2}} \cdot D_{\mathrm{O_2,k}}}{D_{\mathrm{O_2\text{-}N_2}} + D_{\mathrm{O_2,k}}}$ for the cathode; ε is the electrode porosity; θ is the electrode tortuosity; $D_{\mathrm{H_2\text{-}H_2O}}$ stands for the binary diffusion coefficient of H_2 and H_2O, and $D_{\mathrm{O_2\text{-}N_2}}$ for O_2 and N_2; $D_{\mathrm{H_2,k}}$ and $D_{\mathrm{O_2,k}}$ are Knudsen diffusion coefficient of H_2 and O_2, respectively. $\delta_{\mathrm{O_2}}$ equals to $\frac{\frac{\varepsilon}{\theta} \cdot D_{\mathrm{O_2,k}}}{D_{\mathrm{c}}^{\mathrm{eff}} + \frac{\varepsilon}{\theta} \cdot D_{\mathrm{O_2,k}}}$.

The transient response of electrochemistry and fuel processor inside the SOFC (Fig. 1) is modeled to predict the SOFC dynamic behaviors. As is shown in Eq. (7), the corresponding time constant τ_{c} is reported to be 0.8 s [39].

$$V_{\mathrm{CDL}} = V_{\mathrm{act}} + V_{\mathrm{conc}} = I_{\mathrm{FC}} \cdot \left(R_{\mathrm{act}} + R_{\mathrm{conc}} \right) \cdot \left(1 - e^{-\frac{t}{\tau_{\mathrm{c}}}} \right) \tag{7}$$

The fuel processor modeling including H_2, O_2, and H_2O can be described in Eqs. (8-10). The response time constant τ for H_2, O_2, and H_2O flow is 26.1, 2.91 and 78.3 s, respectively [40,41].

$$p_{\mathrm{H_2}} = \frac{1}{K_{\mathrm{H_2}}} \cdot \left(\varphi_{\mathrm{H_2,in}} - 2K_r \cdot I_{\mathrm{FC}} \right) \cdot \left(1 - e^{-\frac{t}{\tau_{\mathrm{H_2}}}} \right) \tag{8}$$

$$p_{\mathrm{O_2}} = \frac{1}{K_{\mathrm{O_2}}} \cdot \left(\varphi_{\mathrm{O_2,in}} - K_r \cdot I_{\mathrm{FC}} \right) \cdot \left(1 - e^{-\frac{t}{\tau_{\mathrm{O_2}}}} \right) \tag{9}$$

$$p_{\mathrm{H_2O}} = \frac{1}{K_{\mathrm{H_2O}}} \cdot \left(2K_r \cdot I_{\mathrm{FC}} \right) \cdot \left(1 - e^{-\frac{t}{\tau_{\mathrm{H_2O}}}} \right) \tag{10}$$

2.2.2 HCCI engine modeling

Generally, the HCCI engine generates power through Otto-cycle via compression, combustion, expansion and exhaust strokes in sequence [42]. In our model, the compression and expansion strokes are assumed to be without gas exchange. During the working process of the HCCI engine, the SOFC anode off-gas and oxygen are first mixed to form a homogeneous mixture as the intake fuel, which is compressed for high-efficiency combustion.

The energy balance equations for the components compressor and turbine are written as follows:

$$P_{\mathrm{comp}} \cdot \eta_{\mathrm{ISC}} \cdot \eta_{\mathrm{MEC}} = \phi \cdot \left(h_{\mathrm{out}} - h_{\mathrm{in}}\right) \tag{11}$$

$$P_{\mathrm{turb}} \cdot \eta_{\mathrm{IST}} \cdot \eta_{\mathrm{MET}} = \phi \cdot \left(h_{\mathrm{out}} - h_{\mathrm{in}}\right) \tag{12}$$

where P_{comp} and P_{turb} stand for the power of compressor and turbine, respectively; η_{ISC} and η_{IST} are the isentropic efficiency of compressor and turbine, and η_{MEC} is the mechanical efficiency, respectively. ϕ is the molar flow; h_{out} and h_{in} are the specific enthalpy of outlet and inlet, respectively.

The energy equation over the combustor can be described in Eq. (13).

$$\phi_{\mathrm{fu}} \cdot h_{\mathrm{fu}} + \phi_{\mathrm{ox}} \cdot h_{\mathrm{ox}} = \phi_{\mathrm{as}} \cdot h_{\mathrm{as}} + \phi_{\mathrm{exh}} \cdot h_{\mathrm{exh}} \tag{13}$$

The relationship between combustion reaction heat and outlet temperature of the combustor during the combustion process can be expressed by Eq. (14).

$$T_{\mathrm{out}} \cdot \phi_{\mathrm{fu}} \cdot \overline{C_p} = \phi_{\mathrm{a,in}} \cdot h_{\mathrm{a,in}} + \phi_{\mathrm{c,in}} \cdot h_{\mathrm{c,in}} - Q_{\mathrm{comb}} \tag{14}$$

where T_{out} is the outlet temperature of the combustor and Q_{comb} is the combustion reaction heat.

The net power output P_{Engine} can be calculated in Eq. (15) according to the thermodynamic cycle:

$$P_{\mathrm{Engine}} = \phi_{\mathrm{fu}} \cdot \left[\left(h_{\mathrm{comb}} - h_{\mathrm{ex}}\right) - \left(h_{\mathrm{comp}} - h_{\mathrm{in}}\right)\right] \tag{15}$$

where P_{Engine} is the engine power; h_{in} and h_{ex} represent the specific enthalpy of inlet fuel and exhaust gas, respectively; h_{comp} and h_{comb} are the specific enthalpy of the fuel gas after the isentropic compression and the isochoric combustion, respectively, which can be calculated by $h_T = h_f + \int C_p(T)dT$ at certain temperature. Herein, h_f is the standard enthalpy of formation of the gas; $C_p(T)$ is the function $C_p(T) = A + B \cdot \frac{T}{1000} + C \cdot \left(\frac{T}{1000}\right)^2 + D \cdot \left(\frac{T}{1000}\right)^3 + E / \left(\frac{T}{1000}\right)^2$ of temperature, among which the polynomial coefficients varying with gas type can be found in NIST Chemistry Webbook.

Since the isochoric combustion process is very fast [43], the engine model does not consider the combustion dynamics but only the ignition model for syngas. The modified Knock-integral-approach [44] is used to predict the auto-ignition time of the HCCI engine. The detailed ignition delay time of the engine can be predicted by Eq. (16) [45]:

$$\tau_{\mathrm{ign}} = 3.7 \times 10^{-6} \cdot p^{-0.5} \cdot \phi^{-0.4} \cdot \chi_{\mathrm{O_2}}^{-5.4} \cdot \exp(\frac{52325}{R_{\mathrm{g}} T}) \tag{16}$$

2.2.3 Reforming process modeling

The reforming reactions converting CH_4 into H_2 are usually expressed in the following Eqs. (17) and (18), which represent the endothermic MSR and exothermic WGS reactions, respectively.

$$\mathrm{CH_4 + H_2O \rightarrow CO + 3H_2} \quad \Delta \mathrm{H} = 206\ \mathrm{kJ/mol} \tag{17}$$

$$\mathrm{CO + H_2O \rightarrow CO_2 + H_2} \quad \Delta \mathrm{H} = -41\ \mathrm{kJ/mol} \tag{18}$$

For the reforming reactions, the kinetic rate equations listed in Eqs. (19) and (20) are usually derived from the Langmuir-Hinshelwood model [46]. In this model, the surface reaction is assumed to be the rate-determining step among adsorption, surface reaction, and desorption.

$$r_{\mathrm{MSR}} = k_{\mathrm{MSR}} \cdot \frac{p_{\mathrm{CH_4}} \cdot p_{\mathrm{H_2O}} / p_{\mathrm{H_2}}^{2.5} - p_{\mathrm{CO}} \cdot p_{\mathrm{H_2}}^{0.5} / K_{\mathrm{MSR}}}{DEN^2} \tag{19}$$

$$r_{\mathrm{WGS}} = k_{\mathrm{WGS}} \cdot \frac{p_{\mathrm{CO}} \cdot p_{\mathrm{H_2O}} / p_{\mathrm{H_2}} - p_{\mathrm{CO_2}} / K_{\mathrm{WGS}}}{DEN^2} \tag{20}$$

among which, the reaction constant (*k*), reaction equilibrium constant (*K*), and the non-dimensional coefficient (*DEN*) are calculated as below [47–50]:

$$k = A \cdot \exp(-\frac{E_{\mathrm{act}}}{R_{\mathrm{g}} T}) \tag{21}$$

$$
\begin{aligned}
\log K_{\mathrm{MSR}} &= f\left(T\right) \\
&= -2.63121\times10^{-11}\cdot T^{4} + 1.24065\times10^{-7}\cdot T^{3} - 2.25232\times10^{-4}\cdot T^{2} + 0.195028\cdot T - 66.1395 \\
\log K_{\mathrm{WGS}} &= f\left(T\right) \\
&= 5.47301\times10^{-12}\cdot T^{4} - 2.57479\times10^{-8}\cdot T^{3} + 4.63742\times10^{-5}\cdot T^{2} - 0.03915\cdot T + 13.2097
\end{aligned}
\qquad (22)
$$

$$
DEN = \frac{1 + L_{\mathrm{CO}}\cdot p_{\mathrm{CO}} + L_{\mathrm{H_2}}\cdot p_{\mathrm{H_2}} + L_{\mathrm{CH_4}}\cdot p_{\mathrm{CH_4}} + L_{\mathrm{H_2O}}\cdot p_{\mathrm{H_2O}}}{p_{\mathrm{H_2}}} \qquad (23)
$$

where the adsorption constant L_i is $L_i = A_i\cdot\exp(-\Delta H_i/(R_{\mathrm{g}}\cdot T))$.

2.2.4 Compressor and heat exchanger modeling

The power consumption of the compressor (W_{comp}) and the corresponding outlet temperature of the compressed gas (T_{out}) are calculated in Eqs. (24) and (25), respectively.

$$
T_{\mathrm{out}} = T_{\mathrm{in}} + T_{\mathrm{in}}\left(\gamma^{\frac{R_{\mathrm{g}}}{C_p}} - 1\right)\cdot\frac{1}{\eta_{\mathrm{ISC}}\cdot\eta_{\mathrm{MEC}}} \qquad (24)
$$

$$
W_{\mathrm{comp}} = \phi\cdot C_p\cdot T_{\mathrm{in}}\left(\gamma^{\frac{R_{\mathrm{g}}}{C_p}} - 1\right)\cdot\frac{1}{\eta_{\mathrm{ISC}}\cdot\eta_{\mathrm{MEC}}} \qquad (25)
$$

The energy equation over the heat exchanger can be described in Eq. (26):

$$
\phi_{\mathrm{hot}}C_{p,\mathrm{hot}}(T_{\mathrm{h}} - T_{\mathrm{l}}) = \phi_{\mathrm{cool}}C_{p,\mathrm{cool}}(T_{\mathrm{h}} - T_{\mathrm{l}}) \qquad (26)
$$

Finally, the overall energy conversion efficiency of the SOFC-HCCI engine hybrid energy conversion system can be calculated by Eq. (27):

$$
\eta = \frac{P_{\mathrm{FC}} + P_{\mathrm{Engine}}}{\phi_{\mathrm{fu}}\cdot LHV_{\mathrm{fu}}} \qquad (27)
$$

2.3. Computational details and model validation

Since the feedback effect of the output power on the input signal is not considered in this work, the overall dynamic response of the hybrid system is a kind of open-loop response. In the present study, MATLAB/SIMULINK is used to perform the dynamic modeling of the hybrid system. The acceptable relative tolerance is set as 0.001. The SIMULINK model solver chooses ode45 algorithm with variable step size. The simulation start time is 0 s and the stop time is 10 s. Besides, some important parameters [21,51–53] used in the overall dynamic model of the hybrid system are listed in Table 1.

Table 1 Some important parameters used for modeling the hybrid system [21,51–53].

Parameter	Value
Operating pressure of the SOFC, p_{FC} (bar)	1.013
Equilibrium pressure of the DIR reaction, p_{reform} (bar)	1.013
Anode thickness, l_a (mm)	1
Electrolyte thickness, l_e (mm)	8×10^{-3}
Cathode thickness, l_c (mm)	20×10^{-3}
Electrode porosity, ε	0.48
Electrode tortuosity, θ	5.4
Cell active area A, cm^2	144
SOFC fuel utilization, μ_{FC}	0.50
Steam to carbon ratio, S/C	2.5
Valve molar constant for H_2, K_{H_2} (mol/(s atm))	0.843
Valve molar constant for O_2, K_{O_2} (mol/(s atm))	2.52
Valve molar constant for H_2O, K_{H_2O} (mol/(s atm))	0.281
Constant $K_r = N/4F$, (mol/(s A))	0.00529
DC/AC conversion efficiency, $\eta_{DC/AC}$	0.96
Isentropic efficiency of compressor, η_{ISC}	0.8
Mechanical efficiency of compressor, η_{MEC}	0.90
Isentropic efficiency of turbine, η_{IST}	0.80

Mechanical efficiency of turbine, η_{MET}	0.90
Generator efficiency, η_{GEN}	0.90
Ex-reforming temperature, $T_{\mathrm{ex\text{-}ref}}$ (K)	823
SOFC-DIR operating temperature, T_{SOFC} (K)	1073
Compression ratio in the engine, γ	4.4
Equivalence ratio, φ	0.9
Operating rotate speed, ω (rpm)	1800
Molar flow of NG, ϕ_{NG} (mol/s)	0.50

Due to the lack of experimental data of system level in the current literature, it is hard to directly validate the dynamic behaviors of the SOFC-Engine hybrid system. Since the hybrid system is mainly composed of the SOFC and the engine, the model validation is performed on the components level of SOFC and engine by comparing the simulation results with experimental data. For the SOFC component, the performance of the fuel cell is closely associated with the polarization curve normally. Therefore, the validation of polarization curves at different operating conditions by experimental data is widely used for the SOFC model validation [22,23]. Fig. 3a displays the comparison of polarization curves between the simulation results and the experimental data [53] at different temperatures, which shows good agreement, validating the present SOFC model. Compared with the SOFC, the internal combustion engine usually has faster dynamic behavior, which mainly depends on the ignition delay time. Therefore, the ignition delay time at different temperatures is also validated for the HCCI engine model by experimental data [45] in this work. The good consistency between simulation and experiment also appears in the HCCI engine component, as shown in Fig. 3b. Therefore, it can be concluded that the established dynamic model in this work is accurate enough to predict the SOFC-Engine hybrid system performance.

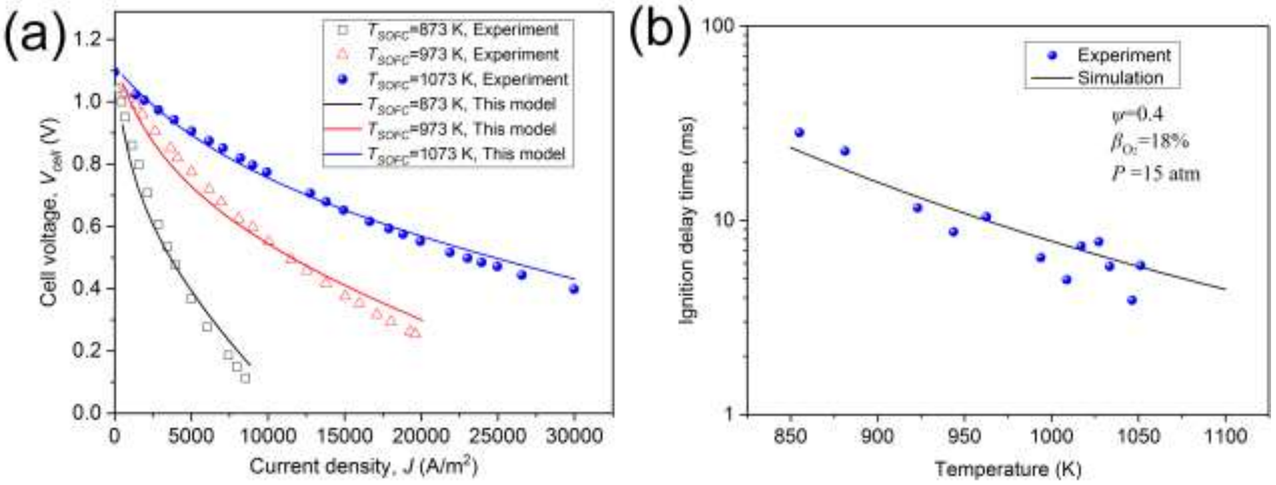

Fig. 3. The model validation. (a) SOFC component; (b) Engine component

3. Results and discussion

3.1. System performance evaluation

As shown in Fig. 4, the SOFC exhibits an inertia effect response, while the HCCI engine presents a delay effect response with the ignition delay time constant τ_{ign}=0.192 s in the model. For the SOFC, it takes about 1.31 s to reach 63.2% of the maximum power. So, the inertia time constant is τ_T=1.31 s, much longer than the time constant of the engine. By comparison, it can be found that the dynamics of the engine is faster than that of the SOFC. Actually, the previous report has indicated that the internal combustion engine generally has fast dynamics due to high operating rotational speed and instantaneous combustion [54]. On the contrary, the dynamic responses of the SOFC are usually slow due to high operating temperatures [55].

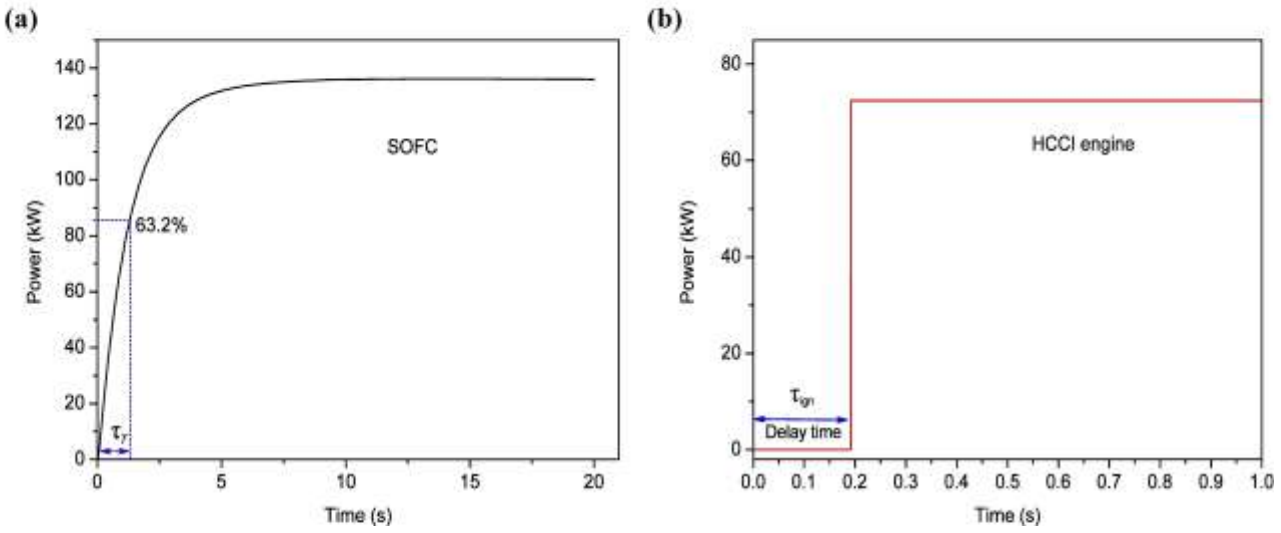

Fig. 4 Dynamic behaviors of the individual SOFC and HCCI engine. (a) SOFC; (b) HCCI engine

However, the engine component in the hybrid system has different dynamic behaviors compared with an individual engine. Fig. 5 shows the dynamic behaviors of the SOFC-Engine hybrid system and the HCCI engine component. The ignition delay time constant of the engine component is reduced to 0.05 s, but an obvious overshoot with the value of σ=66.3% appears after the ignition delay. It needs more than 5 s to reach the stable power output from the engine. The change in the dynamics is mainly attributed to the engine fuel coming directly from the SOFC off-gas in the hybrid system. Namely, the dynamics of the engine depends on the fuel consumption inside the SOFC, especially H_2. It is found that the molar flow of H_2 production for the engine reduces from the maximum to the stable value in more than 5 s, which is determined by the H_2 consumption in the SOFC, as shown in Fig. 5b. The dynamic of H_2 consumption in the SOFC accounts for the overshoot (σ) of the engine power. Therefore, the autonomy of the dynamics for the engine is partly restricted in the hybrid system. In such a situation, the SOFC-Engine hybrid system can output the maximum power of ~210 kW with the energy conversion efficiency of 52.5% after over 5 s. When the hybrid system reaches the stable output, the fuel compositions of the engine are calculated to be 4.74% H_2, 0.08% CH_4, 2.02% CO, 0.85% CO_2, 74.79% N_2, and 17.52% O_2. The corresponding power ratio of the engine to the hybrid system is approximately 34%.

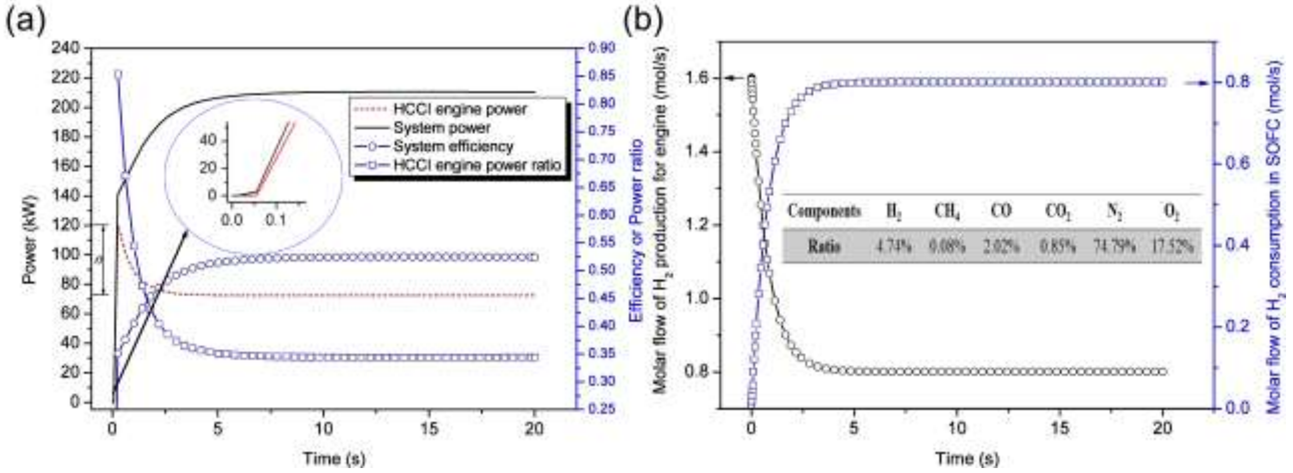

Components	H_2	CH_4	CO	CO_2	N_2	O_2
Ratio	4.74%	0.08%	2.02%	0.85%	74.79%	17.52%

Fig. 5 Dynamic behaviors of the SOFC-Engine hybrid system. (a) Power and efficiency; (b) molar flow of H_2

Fig. 6 displays the effects of SOFC-DIR operating temperatures (873~1073 K) on the hybrid system performance. The power and dynamic are significantly improved at higher operating temperatures. Moreover, a higher temperature usually leads to a larger power output for the engine. A higher SOFC operating temperature also means a higher DIR temperature and more combustible fuel compositions for the engine. As indicated in Fig. 6b, the whole reforming ratio including external and internal reforming reactions is remarkably increased from 55.2% to 97.1% with the operating temperature increasing from 873 to 1073 K. Accordingly, the molar flow of the combustible fuel compositions increases from 0.82 to 1.16 mol/s. Especially, at 1073 K, the amount of CH_4 in the SOFC anode off-gas remains about 0.014 mol/s, indicating that CH_4 has been almost consumed in the SOFC. More combustible fuel compositions account for larger engine power. Consequently, a higher SOFC operating temperature leads to larger SOFC and engine power outputs.

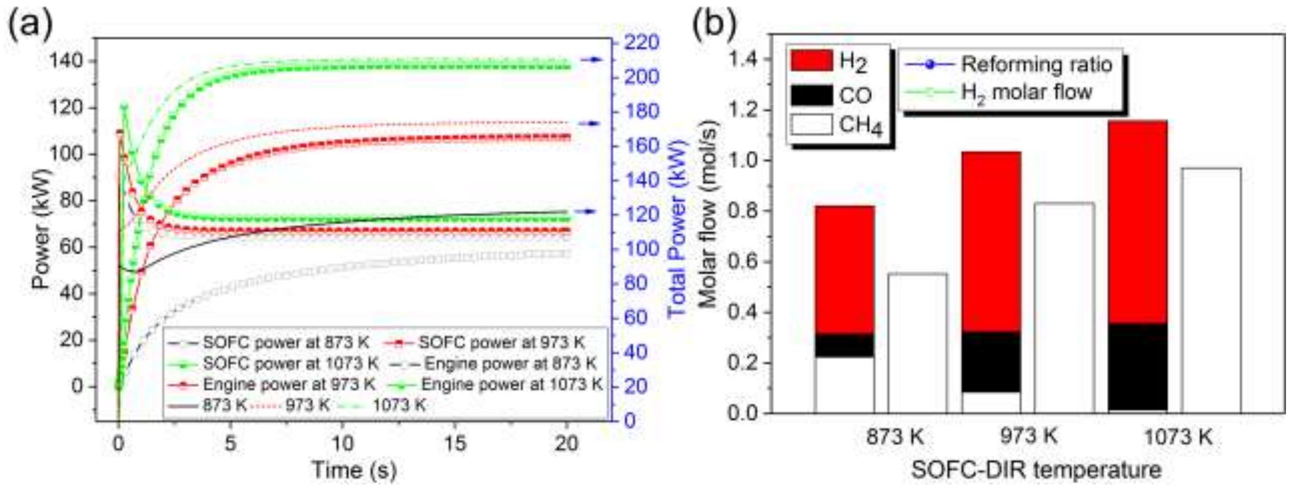

Fig. 6 Effects of SOFC-DIR operating temperatures on the performance of the hybrid system. (a) Power; (b) Molar flow of fuel compositions and reforming ratio

The SOFC-DIR operating temperature also has an impact on the dynamics of the hybrid system. Table 2 lists the dynamic time constants of the SOFC and engine components at different temperatures. The SOFC dynamics is significantly improved at higher temperatures (3.21 s reducing to 1.31 s), while the engine dynamics becomes a little worse (0.0104 s increasing to 0.192 s). Since the temperature effect on the SOFC is much larger than that on the engine, the overall dynamic of the hybrid system is still improved, as illustrated in Fig 6a. The hybrid system can reach a stable power output within about 5 s at 1073 K. By comparison, the system at 873 K needs more than 10 s, which is twice longer.

Table 2 Comparison of dynamics time constant of the SOFC and HCCI engine components at different SOFC-DIR operating temperatures

SOFC-DIR temperature (K)	873	973	1073
Inertia time constant of SOFC (s)	3.21	1.77	1.31
Ignition delay time constant of HCCI engine (s)	0.0104	0.0339	0.192

3.2. H_2 addition optimization

3.2.1 Thermodynamic evaluation of the hybrid system with hydrogen addition

As shown in Fig. 5b, the amount of H_2, which is the major combustible component in the engine fuel, is only 4.74% in volume. The low concentration means the considerably lean fuel for the engine, which is hard to ignite and may cause no combustion in the chamber. Besides, the low H_2 concentration also results in the small power generation for the engine, indicating the relatively small power ratio and low efficiency of the engine in the hybrid system. The power ratio of the engine to the hybrid system in the stable output stage is approximately 34%, and the conversion efficiency of the engine is as low as 24%. This explains why the conversion efficiency of the hybrid system with a high-efficiency SOFC is still less than 60%. On the other hand, the whole fuel of the engine component comes from the SOFC off-gas, indicating that the autonomy of the dynamics for the engine is partly restricted in the hybrid system. Although the engine has fast dynamic behaviors, it is somewhere dominated by the SOFC with the relatively slow dynamic, leading to the dissatisfactory dynamic behaviors of the hybrid system.

To improve the energy conversion efficiency and the dynamic of the hybrid system, the strategy of H_2 addition into the engine by metal hydride reactor (MHR) and waste heat recovery (WHR) unit is introduced. The H_2 addition χ (χ=0, 0.5, 1.0, 1.5 and 2.0), defined as the ratio of the additive H_2 amount to the pristine H_2 amount of the engine fuel, is considered in this work. The working principle of MHR and WHR unit is that metal hydrides can reversibly absorb and desorb H_2 at a certain temperature heated by the waste heat of the exhaust gas. Herein, the typical AB_5-type metal hydrides, which have been widely commercialized, are used as the H_2 addition medium. This kind of metal hydride has a high hydrogen absorption/desorption cycles up to 18180 times due to the relatively small lattice expansion/shrinkage in the hydrogen storage process [56]. The cycle life is much higher than the value (1500 cycle/5000 h) for the on-board hydrogen storage goal (U.S. Department of Energy [57]). That is to say, this kind of metal hydride has a long life duration as H_2 addition medium can be a promising candidate from the point of cycle life. The reversible hydrogen absorption/desorption reaction of AB_5-type metal hydride can be written in Eq. (28) [58]:

$$\mathrm{LaNi_5} + 3\mathrm{H_2} \rightleftarrows \mathrm{LaNi_5H_6} + \Delta H \tag{28}$$

Actually, the waste heat value of the engine exhaust gas is large enough to support the MHR releasing H_2 via endothermic reaction for the engine, which is found to be 228.8 kW, while the largest reaction heat required for the H_2 desorption from the MHR is 48.2 kW at χ=2.0, as listed in Table 3. Moreover, the temperature of the exhaust gas under the condition of a fixed stack gas temperature of 333 K is calculated to be ~562 K, much higher than the required MHR reaction temperature (less than 373 K). Therefore, it is feasible to achieve the H_2 addition into the engine by recycling the engine waste heat to drive the H_2 desorption from the MHR. In addition, it is found that the H_2 addition helps to improve the overall conversion efficiency of the hybrid system. As illustrated in Fig. 7, the overall energy conversion efficiency asymptotically increases from 52.5 % to 67.6% with the H_2 addition χ increasing from 0 to 2.0. It should be noted that the heat value of H_2 addition by the typical AB_5-type MH was reported to account for around 12% of the LHV of hydrogen [59]. The LHV of the new fuel after H_2 addition varies with different values of the H_2 addition χ. When the χ is set as 1.38, the HCCI engine has the same power output as the SOFC with the power of 138 kW. In this case, the efficiency of the hybrid system reaches up to 63.7%. Although the H_2 addition directly for the SOFC fuel can also increase the efficiency, there is still a large amount of waste heat accompanying the SOFC off-gas. Thus, the H_2 addition into the SOFC has few impacts on improving the thermal efficiency, causing the relatively low efficiency of the standalone SOFC. In contrast, the HCCI engine subsystem is to make full use of the SOFC waste heat and unconsumed fuel for additional power generation. The H_2 addition into the HCCI engine was found to effectively improve the efficiency of waste heat converting to power. The overall efficiency (~61%) of H_2 addition for the ICE in the hybrid system is a little higher than the value (~59%) for the SOFC at the same H_2 addition χ=1.0. Compared with the way of using the waste heat of SOFC off-gas to drive MHR to desorb hydrogen for SOFC, the method of H_2 addition into the engine by recycling the waste heat from the engine to drive the H_2 desorption from the MHR has a preferable energy conversion efficiency. This is because that the fuel utilization ratio of engine is higher than that of SOFC. The hydrogen added into the engine can be almost completely burned and thermal energy can be fully released when the engine is running smoothly.

Table 3 The required MHR reaction heat and temperature under different H_2 addition χ and the waste heat of the exhaust gas

H_2 addition	χ=0	χ=0.5	χ=1.0	χ=1.5	χ=2.0
H_2 molar flow (mol/s)	0	0.40045	0.8009	1.20135	1.6018
MHR reaction heat (kW)	0	12.05	24.10	36.15	48.20
Exhaust gas heat value (kW)			228.8		
MHR reaction temperature (K)			>303		
Exhaust gas temperature (K)			~562		

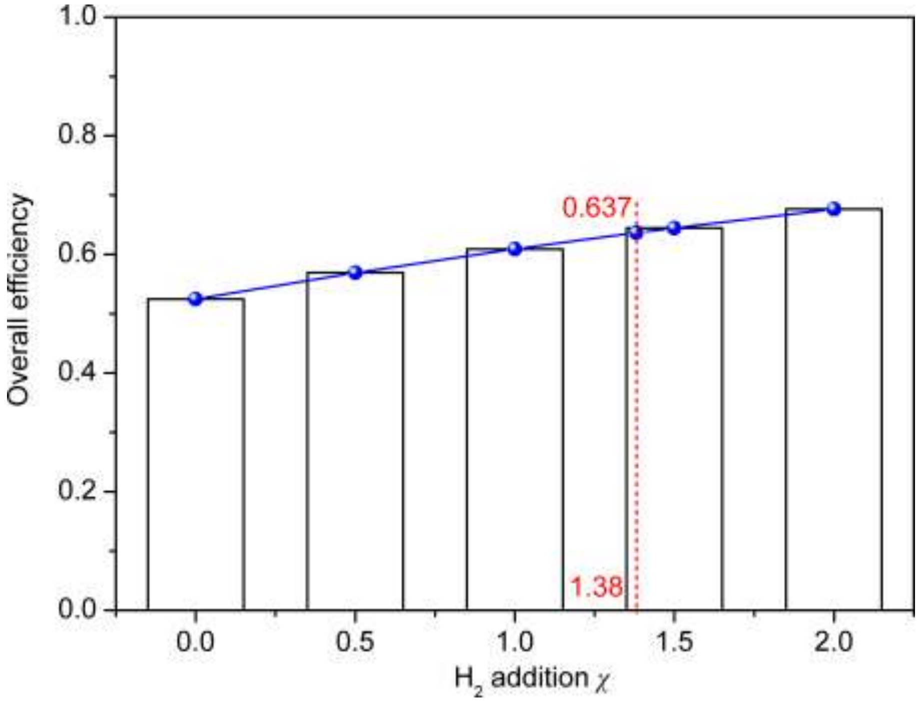

Fig. 7 The overall energy conversion efficiency of the hybrid system at different H_2 addition χ

3.2.2 Dynamic analysis of the hybrid system with hydrogen addition

Fig. 8 shows the effect of H_2 addition χ on the dynamic properties of the HCCI engine. As more H_2 is added into the engine, the stable output power of the engine varies from 81.7 to 165.6 kW. This is because the H_2 amount in the engine fuel increases from 4.74% to 12.97%, as listed in Table 4.

Accordingly, the amount of combustible gas compositions increases from 6.84% to 14.89%, indicating more combustion heat is generated in the engine and leads to more power output. Moreover, the overshoot and the ignition delay time gradually decrease from 68.3% to 56.2% and from 0.162 to 0.0594 s, respectively. These results suggest that the addition of H_2 fuel contributes to enhancing the dynamic behaviors of the engine.

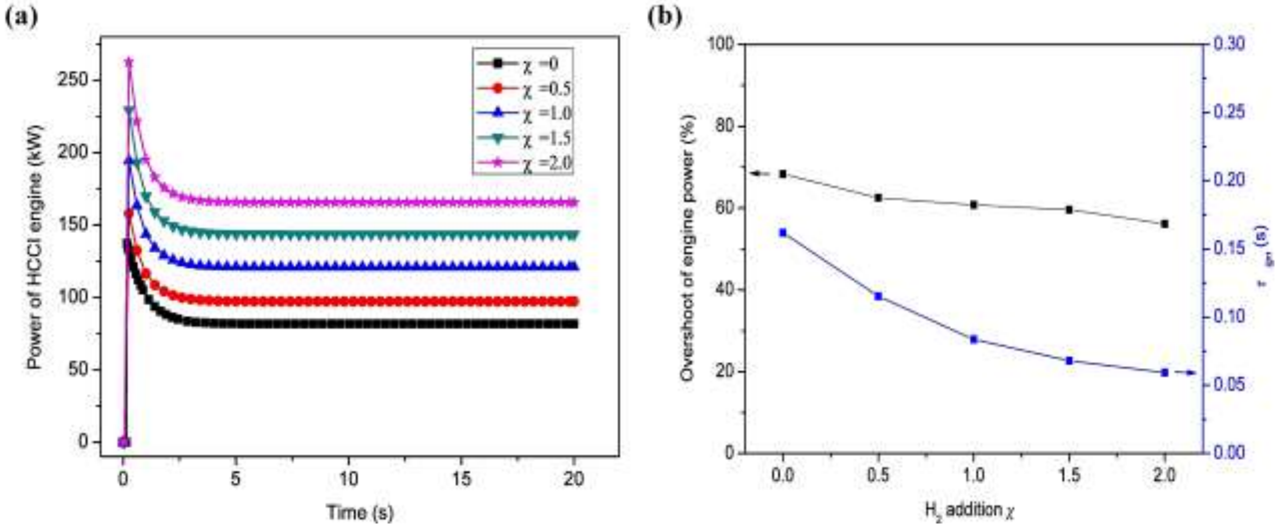

Fig. 8 The dynamics of the HCCI engine component in different H_2 addition χ. (a) Power; (b) Overshoot and delay time constant

Table 4 Fuel compositions of HCCI engine with different H_2 addition χ

Compositions	H_2	O_2	CH_4	CO	CO_2	N_2
χ=0	4.74%	17.52%	0.08%	2.02%	0.85%	74.79%
χ=0.5	6.94%	17.11%	0.08%	1.97%	0.83%	73.07%
χ=1.0	9.04%	16.73%	0.08%	1.92%	0.82%	71.41%
χ=1.5	11.05%	16.35%	0.08%	1.88%	0.80%	69.84%
χ=2.0	12.97%	16.00%	0.08%	1.84%	0.78%	68.33%

Fig. 9a shows the effect of H_2 addition on the dynamic behaviors of the hybrid system. The response of the hybrid system becomes slower after the H_2 addition by the MHR. It takes more than 100 s to reach the stable power output for both the hybrid system and the engine component, which is far longer than that without H_2 addition (5 s). This is mainly because the H_2 desorption reaction occurring in the MHR is a gas-solid reaction with generally slow reaction kinetics. Even at a high temperature of 373 K, the time constant of the MHR hydrogen desorption reaction still reaches 38.6 s. The gas-solid reaction dynamics of the $LaNi_{4.3}Al_{0.7}$ metal hydride for hydrogen desorption can be described in Eq. (29) [58]. For the MHR simulation, the governing equations of mass and energy conservation are written in Eqs. (30-33). The values of the main parameters used in the dynamic model of the MHR are also summarized in Table 5.

$$\dot{m}_{\mathrm{H_2}} = C_{\mathrm{d}} \cdot \exp(-\frac{E_{\mathrm{act}}}{R_{\mathrm{g}} T_{\mathrm{MHR}}}) \cdot \left(\frac{p_{\mathrm{g}} - p_{\mathrm{eq}}}{p_{\mathrm{eq}}} \right) \cdot \left(\rho_{\mathrm{MH}} - \rho_{\mathrm{HSA}} \right) \tag{29}$$

Mass conservation equations:

$$\varepsilon \frac{\partial \rho_{\mathrm{g}}}{\partial t} = \overset{\bullet}{m}_{\mathrm{H_2}} \quad \text{for } \mathrm{H_2} \tag{30}$$

$$(1-\varepsilon) \frac{\partial \rho_{\mathrm{s}}}{\partial t} = -\overset{\bullet}{m}_{\mathrm{H_2}} \quad \text{for porous MH bed} \tag{31}$$

where ε is the porosity of the MH bed; ρ_{g} and ρ_{s} are densities of hydrogen gas and the MH, respectively; $\overset{\bullet}{m}_{\mathrm{H_2}}$ stands for hydrogen desorption rate.

Energy conservation equations [60,61]:

$$(\rho C_p)_{\mathrm{eff}} \frac{\partial T}{\partial t} = \nabla \cdot (\lambda_{\mathrm{eff}} \nabla T) + \overset{\bullet}{m} \frac{\Delta H}{M_{\mathrm{g}}} \quad \text{for MH bed} \tag{32}$$

$$Q = h_{\mathrm{f}} \cdot A_{\mathrm{HE}} \cdot (T_{\mathrm{w}} - T_{\mathrm{MHR}}) \quad \text{for heat exchange tube} \tag{33}$$

where $(\rho C_p)_{\mathrm{eff}} = \varepsilon \rho_{\mathrm{g}} C_{p,\mathrm{g}} + (1\text{-}\varepsilon) \rho_{\mathrm{MH}} C_{p,\mathrm{MH}}$ is the effective volumetric heat capacity; $\lambda_{\mathrm{eff}} = \varepsilon \lambda_{\mathrm{g}} + (1-\varepsilon) \lambda_{\mathrm{MH}}$ is the effective thermal conductivity; M_{g} is the molar mass of hydrogen gas; ΔH stands for the reaction heat; T_{w} is the temperature of heat transfer fluid; h_{f} is the coefficient of heat transfer between the MHR and the heat transfer fluid; A_{HE} is the heat transfer area.

Table 5 The thermal-physical parameters used in the MH dynamic model [58,62–64]

Parameters	Values
Rate constant for desorption, C_d	9.57 s^{-1}
Activation energy for desorption, E_d	16473.59 J mol^{-1}
Reaction enthalpy, ΔH	±30100 J mol^{-1}
Density of saturated MH, ρ_MH	8527 kg m^{-3}
Density of hydrogen-free MH, ρ_HSA	8400 kg m^{-3}
Thermal conductivity of MH with expanded graphite, λ_{MH}	10.00 W $(\mathrm{m\ K})^{-1}$
Specific heat of MH, $C_{p,\mathrm{MH}}$	419 J $(\mathrm{kg\ K})^{-1}$
Porosity of MH, ε	0.5
Desorption temperature, T_MHR	353~373 K
Hydrogen pressure, p_g	0.085 bar
Molar mass of hydrogen, M_g	0.002 kg $(\mathrm{mol})^{-1}$
Density of hydrogen, ρ_g	0.32 kg $(\mathrm{m})^{-3}$
Thermal conductivity of hydrogen, λ_g	0.167 W $(\mathrm{m\ K})^{-1}$
Specific heat of hydrogen, $C_{p,\mathrm{g}}$	14890 J $(\mathrm{kg\ K})^{-1}$
Desorption equilibrium pressure, p_eq	$p_\mathrm{eq} = \exp(10.570 - \frac{3704.6}{T_\mathrm{MHR}})$
Temperature of heat transfer fluid, T_w	353~373 K
Coefficient of heat transfer, h_f	1652 W $(\mathrm{m}^2\ \mathrm{K})^{-1}$

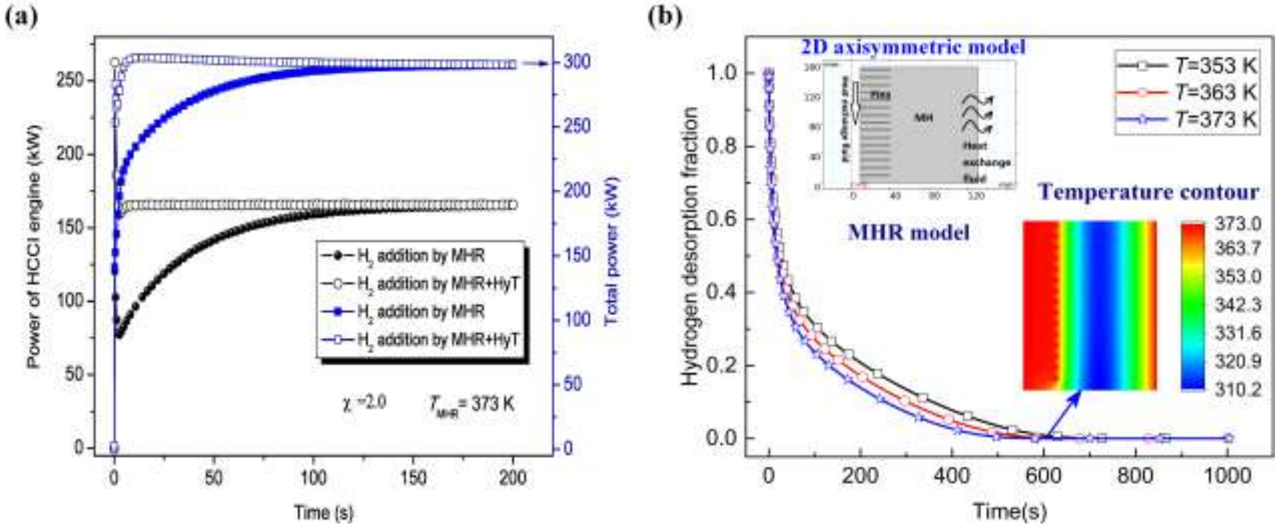

Fig. 9 The dynamics of the hybrid system in different H_2 addition modes. (a) Power of engine component and hybrid system; (b) H_2 desorption kinetics of the MHR at different temperatures

Based on the hydrogen desorption dynamic model of the MHR, the desorption kinetics of the MHR loaded with AB_5-type metal hydride at 353, 363 and 373 K for H_2 release is obtained, as shown in Fig. 9b. Although increasing the hydrogen desorption temperature can improve the hydrogen desorption kinetics, it is very difficult for the MHR to complete desorption process in a short time due to the intrinsic dynamic characteristics of the gas-solid reaction [65,66]. For example, the MHR still needs about 400 s to release most of H_2 at the temperature of 373 K with considering of the superior heat management, as illustrated in the inset graph of Fig. 9b. Therefore, a hydrogen tank (HyT) is incorporated between the MHR and the engine as H_2 buffer to improve the H_2 addition dynamics in this work. In the MHR+HyT mode, the slow H_2 desorption dynamic of the MHR caused by the intrinsic kinetics of the gas-solid reaction is replaced by the fuel intake dynamics of the HyT, which is generally viewed to be fast in fact. In such a case, the dynamics of the hybrid system can be remarkably improved, as illustrated in Fig. 9a. Therefore, the MHR+HyT mode is suggested for H_2 addition in the hybrid system.

Fig. 10a illustrates the dynamic performance of the hybrid system under different H_2 addition χ. After the H_2 addition, the total output power increases from ~220 to ~300 kW due to the increased engine power. When the value of χ is more than 1.0, the total power first increases and then decreases within the initial 1 s and then gradually increases to a stable value. The difference in the dynamics indicates that the overshoot that usually occurs in the engine component starts to appear in the H_2 addition over 1.0. That is to say, the engine component begins to take effect in the dynamic of the hybrid system owing to the promoted autonomy caused by more H_2 addition. Meanwhile, the power ratio of the HCCI engine also increases to 46.7%~54.5% with χ of 1.0~2.0, as shown in Fig. 10b. Consequently, the engine component has more impact on the dynamic performance of the hybrid system with the increase of H_2 addition by the MHR+HyT. Herein, it should be noted that the range of H_2 addition is not limited to χ=0~2.0, but a higher H_2 addition can also cause the higher component cost, the heavier, the larger, and the more complex power system in the practical applications.

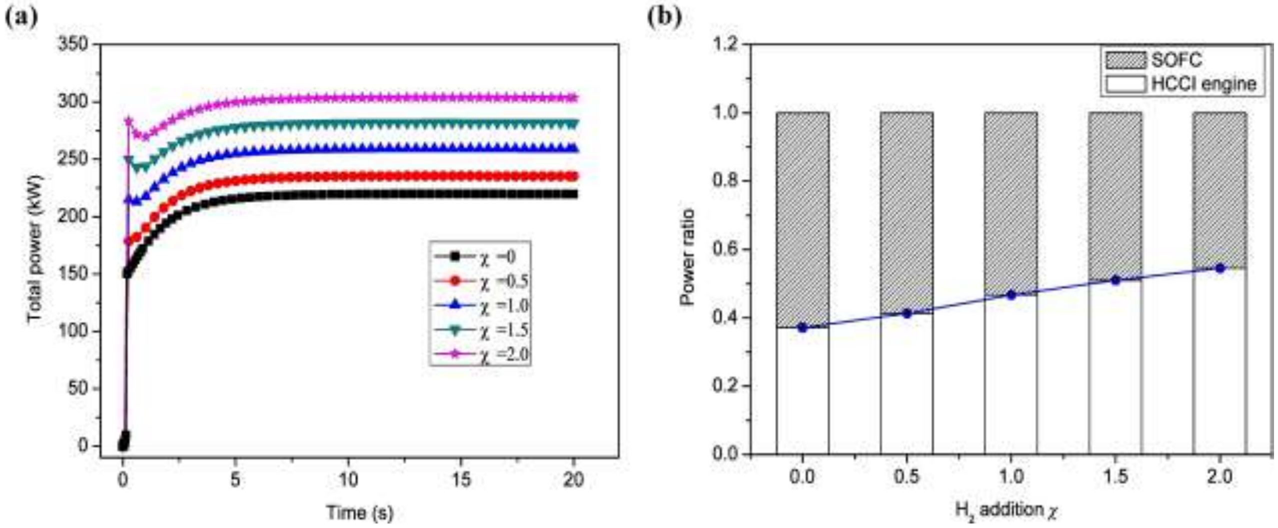

Fig. 10 The dynamics of the hybrid system in different H_2 addition χ. (a) Power; (b) Power ratio

3.2.3 Cost prediction of hydrogen addition system

When the amount of H_2 addition χ is 1.0, the AB_5-type metal hydride of about 70 kg is required to supply the H_2 for the engine. Accordingly, the reactor with a weight of ~40 kg and a volume of ~8 L is employed to load the metal hydride. The volume of the reactor is much smaller than that of a high-pressure H_2 tank, which is usually over 120 L. The total metal hydride reactor as H_2 additional device weighs about 110 kg, which accounts for a small portion of the weight of the vehicles (usually over 1500 kg). The additional cost caused by the H_2 addition is preliminarily estimated in this study. Table 6 lists the cost equations of the main components, including the SOFC, HCCI engine, MHR and the corresponding parameters used in the cost equations for economic estimation [21,67–70]. The estimated component cost and cost ratio are summarized in Table 7. The additional cost (the MHR cost) caused by the H_2 addition increases from 1439 to 5507 $ with an increase of H_2 addition χ from 0.5 to 2.0. Herein, the MHR is composed of stainless steel 316L. The corresponding ratio of the increased additional cost to the total component cost is in the small range of 1.0%~3.9%. However, the energy conversion efficiency is accordingly improved from 52.45% to 67.63%. Therefore, it is worth spending the additional cost of the MHR to supply additional H_2 for the HCCI engine, thus significantly improve the energy conversion efficiency of the SOFC-HCCI engine hybrid power system. Besides, the unit power generation cost of the SOFC reaches up to about 900 \$/kW, which is much higher than the value (~110 \$/kW) of the HCCI engine. Therefore, compared to increasing the SOFC power by H_2 addition, increasing the power of the engine by H_2 addition helps to cut down the cost of power generation.

Table 6 The cost equations of the three main components and the corresponding parameters used in the cost equations [21,67–70]

Component	Cost equation	Parameters
SOFC	$C_{\text{SOFC}} = C_{\text{Stack}} + C_{\text{INV}} + C_{\text{AUX}}$ FC stack: $C_{\text{Stack}} = A_{\text{cell}} \cdot \left(2.96 \cdot T_{\text{SOFC}} - 1907\right)$ Inverter: $C_{\text{INV}} = 10^5 \cdot \left(\frac{W_{\text{SOFC}}}{500}\right)^{0.70}$ Auxiliary: $C_{\text{AUX}} = 0.1 \cdot C_{\text{Stack}}$	Active cell area: $A_{\text{cell}} = 60.70\ \text{m}^2$ Temperature: $T_{\text{SOFC}} = 1073\ \text{K}$ Power: $W_{\text{SOFC}} = 138\ \text{kW}$
HCCI engine	$C_{\text{HCCI}} = V_{\text{HCCI}} \cdot 1.5 \cdot 9293 \cdot \left(V_{\text{HCCI}}\right)^{-0.863}$	Engine cylinder volume: $V_{\text{HCCI}} = 2.0\ \text{L}$
MHR	$C_{\text{H2add}} = C_{\text{MH}} + C_{\text{MHR}}$ $C_{\text{MH}} = \frac{m_{\text{H}_2}}{\psi_{\text{MH}}} \cdot \omega_{\text{MH}}$ $C_{\text{MHR}} = V_{\text{316L}} \cdot \rho_{\text{316L}} \cdot C_{\text{316L}}$	H_2 mass: m_{H_2} H_2 capacity of MH: $\psi_{\text{MH}} = 1.39\ \text{wt\%}$ MH price: $\omega_{\text{MH}} = 37.82\ \$/\text{kg}$ Reactor volume: V_{316L} Density of reactor material 316L: $\rho_{\text{316L}} = 7980\ \text{kg/m}^3$ 316L price: $C_{\text{316L}} = 3.368\ \$/\text{kg}$

Table 7 The estimated component cost and its ratio to the total component cost under different H_2 addition χ

H_2 addition	Efficiency	Component cost ($)			MHR cost ratio
		SOFC	HCCI engine	MHR	
χ=0	52.45%	125347	15328	0	0
χ=0.5	56.93%			1439	1.0%
χ=1.0	60.92%			2795	2.0%
χ=1.5	64.46%			4151	2.9%
χ=2.0	67.63%			5507	3.9%

3.3. Power distribution and control strategy

The SOFC fuel utilization μ_{FC} is set as 0.5 only for ascertaining enough unconsumed fuel for the downstream engine. When the H_2 addition χ is 2.0, the engine fuel and diluent ratio become 23.8% and 76.2%, respectively. According to the fuel compositions of the engine listed in Table 4, the air-fuel ratio is reduced to approximately 7:1 (mass ratio), which is much lower than the value 10~23:1 commonly used for the lean burning engine [71]. Therefore, the SOFC anode off-gas at μ_{FC}=0.5 with the H_2 addition is sufficient to support the HCCI engine for power generation. As an SOFC generally has larger conversion efficiency than an IC engine, increasing the efficiency of the SOFC has larger influences than that of the engine on the overall efficiency improvement of the hybrid system. Considering that the anode off-gas at μ_{FC}=0.5 contains enough combustible gas compositions, the approach of increasing the SOFC fuel utilization is proposed to further improve the overall efficiency of the hybrid system. Herein, the increase of μ_{FC} should take the normal operation of the downstream engine as a prerequisite, since the increased μ_{FC} inevitably causes the reduction in the amount of the combustible gas compositions for the HCCI engine.

The effect of the SOFC fuel utilization (μ_{FC}) on the dynamic performance of the hybrid system is shown in Fig. 11. A higher μ_{FC} value causes the higher overall efficiency. When the μ_{FC} is more than 0.8, the overall energy conversion efficiency almost keeps the same, which is over 71% at χ =1.5. Thus, the overall efficiency of the hybrid system can increase by about 7% by adjusting the fuel utilization. It can be observed from Fig. 11b that the effect of μ_{FC} on the dynamics of the hybrid system is small. Table 8 lists the important dynamics parameters of the SOFC and engine components at different μ_{FC} values. When the μ_{FC} increases from 0.5 to 0.8, the inertia time constant of the SOFC and the delay time constant of the engine increase from 1.31 to 1.33 s and from 0.0681 to 0.0975 s, respectively. The results reveal that the higher value μ_{FC} easily results in the worse dynamics for the hybrid system, but the variation in the time constant is small.

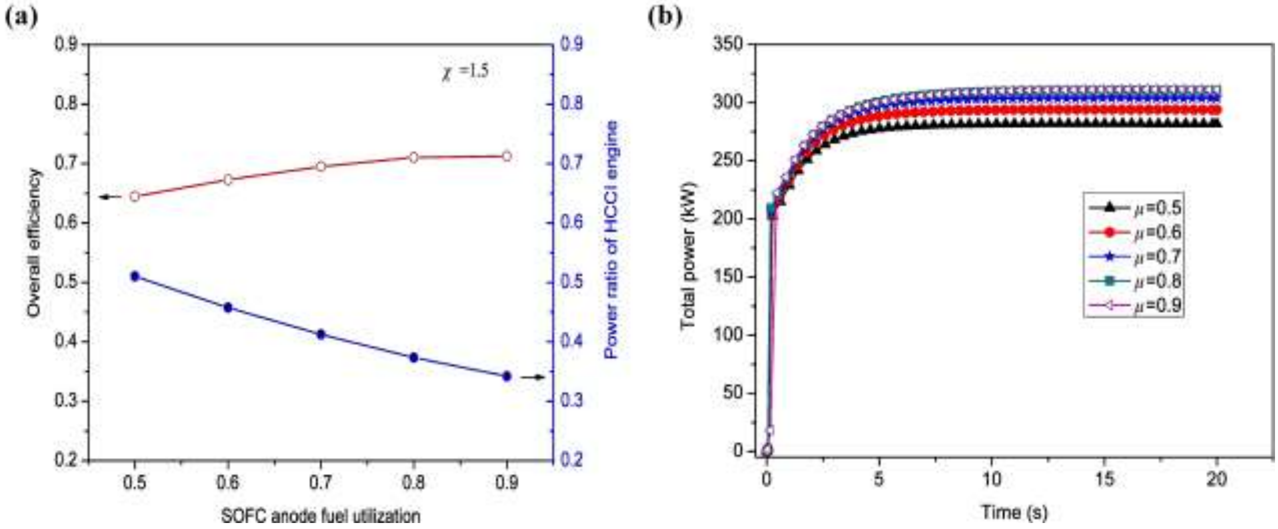

Fig. 11 The performance of the hybrid system in different SOFC fuel utilization μ_{FC}. (a) Overall efficiency and power ratio of HCCI engine; (b) Dynamics response

Table 8 Comparison of dynamics time constant of the SOFC and HCCI engine components at different SOFC fuel utilization μ_{FC}

SOFC fuel utilization	μ_{FC}=0.5	μ_{FC}=0.6	μ_{FC}=0.7	μ_{FC}=0.8	μ_{FC}=0.9
Inertia time constant of SOFC τ_T (s)	1.31	1.32	1.33	1.33	1.29
Ignition delay time constant of HCCI engine τ_{ign} (s)	0.0681	0.0753	0.0848	0.0975	0.115
Overshoot of HCCI engine σ	26.7%	36.3%	48.8%	64.2%	54.6%

As shown in Fig. 11a, the power ratio of the HCCI engine decreases with an increase of μ_{FC} due to the improved SOFC efficiency. The improved efficiency of the hybrid system is attributed to the larger power ratio of the SOFC with high efficiency, while the worse dynamic is because of less power contribution of the engine with fast dynamics. Therefore, the power distribution is crucial for the performance optimization of the hybrid power system [72]. Additionally, the high degree of system complexity indicates that an elaborated control strategy is required for the SOFC-Engine hybrid energy conversion system, which is proposed as follows. First, the fuel utilization is used to regulate the SOFC power according to the required power distribution. Secondly, H_2 addition is used to regulate the remaining engine power. The corresponding schematic diagram is shown in Fig. 12.

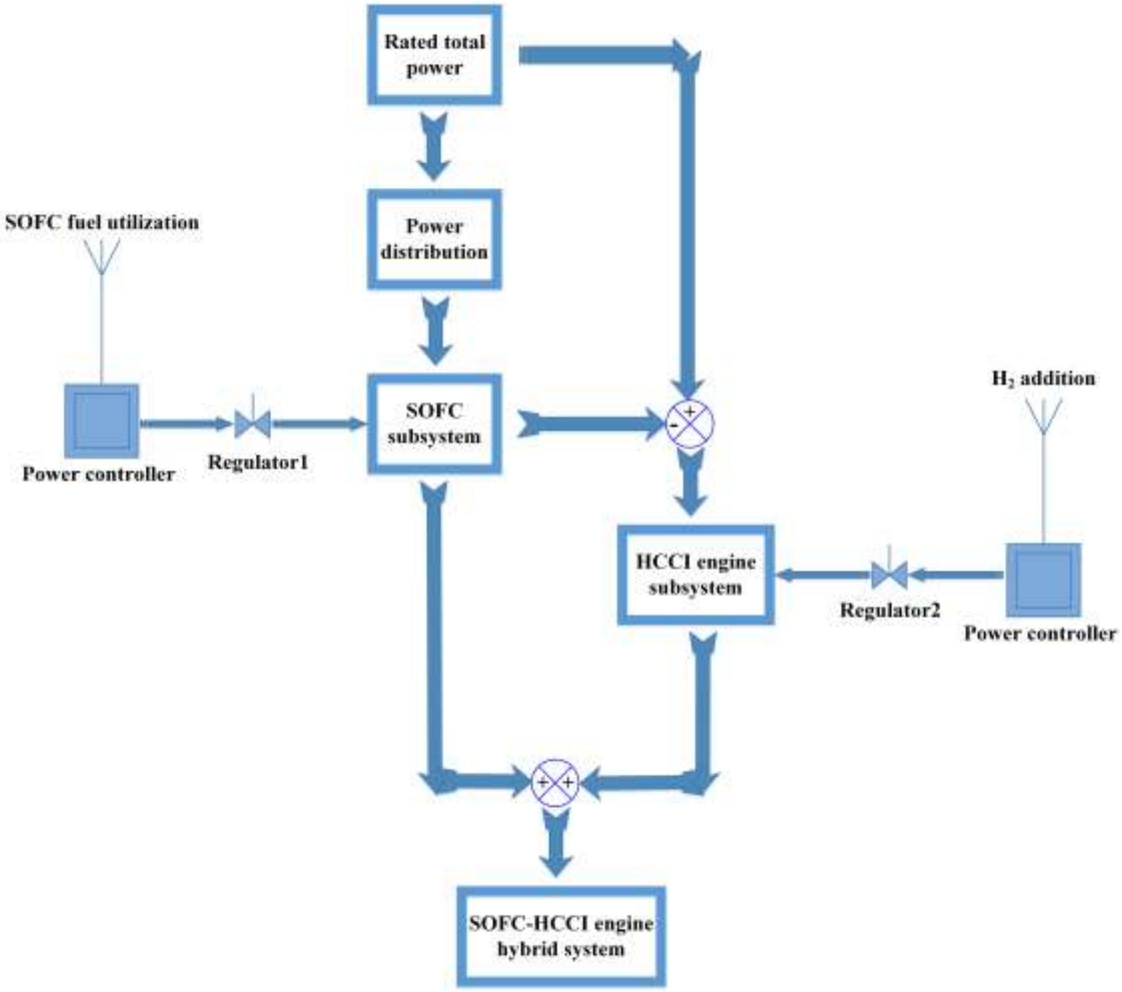

Fig. 12 Schematic diagram of power distribution control strategy

In the present study, the hybrid system with different power distributions between the SOFC and the engine in such a control strategy is modeled to investigate the dynamics. The dynamic of the hybrid system and its main components under the SOFC power ratio varying from 40% to 80% is demonstrated in Fig. 13. The corresponding time constant, required fuel utilization and H_2 addition are also listed in Table 9. The higher SOFC power ratio usually results in the worse engine performance. When the SOFC power ratio increases from 40% to 80%, the delay time constant increases from 0.0636 to 0.403 s and from 15.8% to 134.7% for the overshoot. Accordingly, the response of the hybrid system becomes a little slower. However, the lower power ratio of the SOFC requires more H_2 addition, indicating that more metal hydrides are needed. The cost and complexity degree of the power system will increase accordingly. Therefore, the moderate power distribution of 50%~60% for the SOFC is recommend for the SOFC-Engine hybrid system to achieve a preferable overall performance when the dynamic performance of the system against the effects of the MHR on the system is considered.

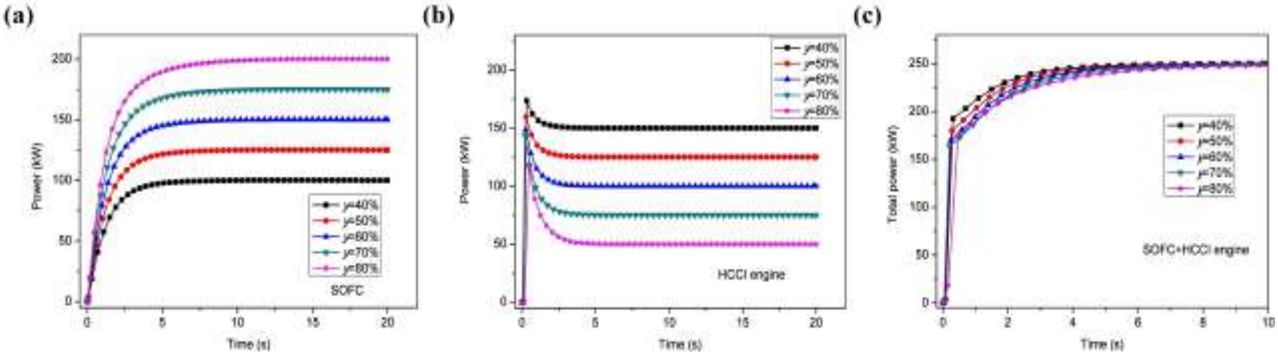

Fig. 13 The dynamics of the hybrid system in different SOFC power ratio y. (a) SOFC; (b) HCCI engine; (c) SOFC-HCCI engine hybrid system

Table 9 Comparison of the required fuel utilization μ_{FC}, H_2 addition χ and the dynamics time constant τ_T and τ_{ign} at different power distribution y

SOFC power ratio	y=0.4	y=0.5	y=0.6	y=0.7	y=0.8
SOFC fuel utilization μ_{FC}	0.3413	0.4435	0.5547	0.680	0.843
H_2 addition χ	0.9992	0.8738	0.7499	0.6425	0.3873
Inertia time constant of SOFC τ_T (s)	1.28	1.30	1.32	1.32	1.32
Ignition delay time constant of HCCI engine τ_{ign} (s)	0.0636	0.0797	0.111	0.181	0.403
Overshoot of HCCI engine σ	15.8%	27.7%	48.5%	91.3%	134.7%

3.4. Dynamic response of the hybrid system to typical driving cycles

In practical mobile applications, besides the superior dynamics, the hybrid system should quickly respond to the change of the power load. Considering of the SOFC with high efficiency but slow dynamics, it can be used to provide most of the hybrid system power as the power baseline, which keeps stable output during the load changes. On the other hand, the engine is used to cope with most of the dynamics because of its fast response. On the basis of such an operation strategy, the transient response of the hybrid power system at different typical driving cycles is further investigated in this work. Herein, the power ratio of SOFC and HCCI engine is set as 60% and 40%, whose output power is 150 kW and 100 kW, respectively. The following four kinds of driving cycles, including start-up, cruise control, speed-up, and variable driving, are generally considered as typical driving cycles. Equations (30-33) describe the expected input power signals to represent the four kinds of driving cycles, respectively. To approximately describe the variable driving conditions, the sine signal with the period of 2 s and the power baseline of 250 kW is employed as the load change signal (input power signal) in this work. Why the period of the input power sine signal is 2 s is selected to study the response characteristics of the system to the sinusoidal input power load is that the period is close to the inertia time constant of SOFC.

$$P_{\text{in\_start}} = \begin{cases} 0 & t = 0\,\text{s} \\ 250 & t > 0\,\text{s} \end{cases} \tag{30}$$

$$P_{\text{in\_cruise}} = 250 \tag{31}$$

$$P_{\text{in\_speed-up}} = \begin{cases} 250 & t < 1\,\text{s} \\ 300 & t \geq 1\,\text{s} \end{cases} \tag{32}$$

$$P_{\text{in\_variable}} = 50 \cdot \sin(\pi \cdot t) + 250 \tag{33}$$

Fig. 14 shows the transient response of the hybrid power system to the four kind of typical driving cycles in such operation strategy. For the start-up driving cycle, it takes about 6 s to achieve the stable power output, as shown in Fig. 14a. The overshoot of 48.5% appears in the HCCI engine component in the first 2 s. At the beginning of start-up cycle, the HCCI engine dominates the dynamic behaviors while the SOFC gradually controls the dynamic response of the hybrid power system after the first 2 s. When the vehicle comes into the cruise control for driving, the SOFC and HCCI engine components consistently and steadily output 150 kW and 100 kW, as shown in Fig. 14b. The corresponding power ratio of SOFC and HCCI engine is 60% and 40%, respectively. When the vehicle needs to speed up, the required power is assumed to change from 250 kW to 300 kW, as shown in Fig. 14c. In this case, the SOFC provides a stable power output of 150 kW, while the HCCI engine copes with the dynamics part. Actually, the input power load is a step signal. It can be seen that the actual output signal of the hybrid system enables to quickly follow the load variation but with a little delay. The delay time constant of the HCCI engine is found to be 0.0662 s and the whole delay time τ is approximately 0.1 s. By comparison, the whole delay time τ increases to 0.16 s for the sine signal at the variable driving cycle, as shown in Fig. 14d. Accordingly, the delay time constant of the HCCI engine increases to be 0.0681 s. It is noted that the time difference between the input and output power signals is different at the peak and trough. The time difference at the peak is $\triangle t_1$=~0.1 s, smaller than the value $\triangle t_2$=~0.32 s at the trough. The hybrid system can quickly follow the load change at the peak while the response is not so good at the trough. It can be found that the higher engine power facilitates the response. If the period of the input signal is greater than 2 s, the output power can certainly meet the dynamic requirements of the system. On the contrary, if the output is a higher step signal with a period less than 2 s, the output power may not follow the change of the input signal. This means that the dynamic performance of the system cannot meet the requirements when the load changes. Actually, for ships, heavy trucks and other large vehicles, the requirements for dynamic characteristics are not very high. A signal with an input period of 2 s can represent a typical operating condition. Besides, the hybrid system can achieve the overall energy conversion efficiency (including thermal efficiency) up to 74.8% during the load change. Therefore, in such an operation strategy, the proposed hybrid power system can achieve relatively fast response and high energy conversion efficiency simultaneously.

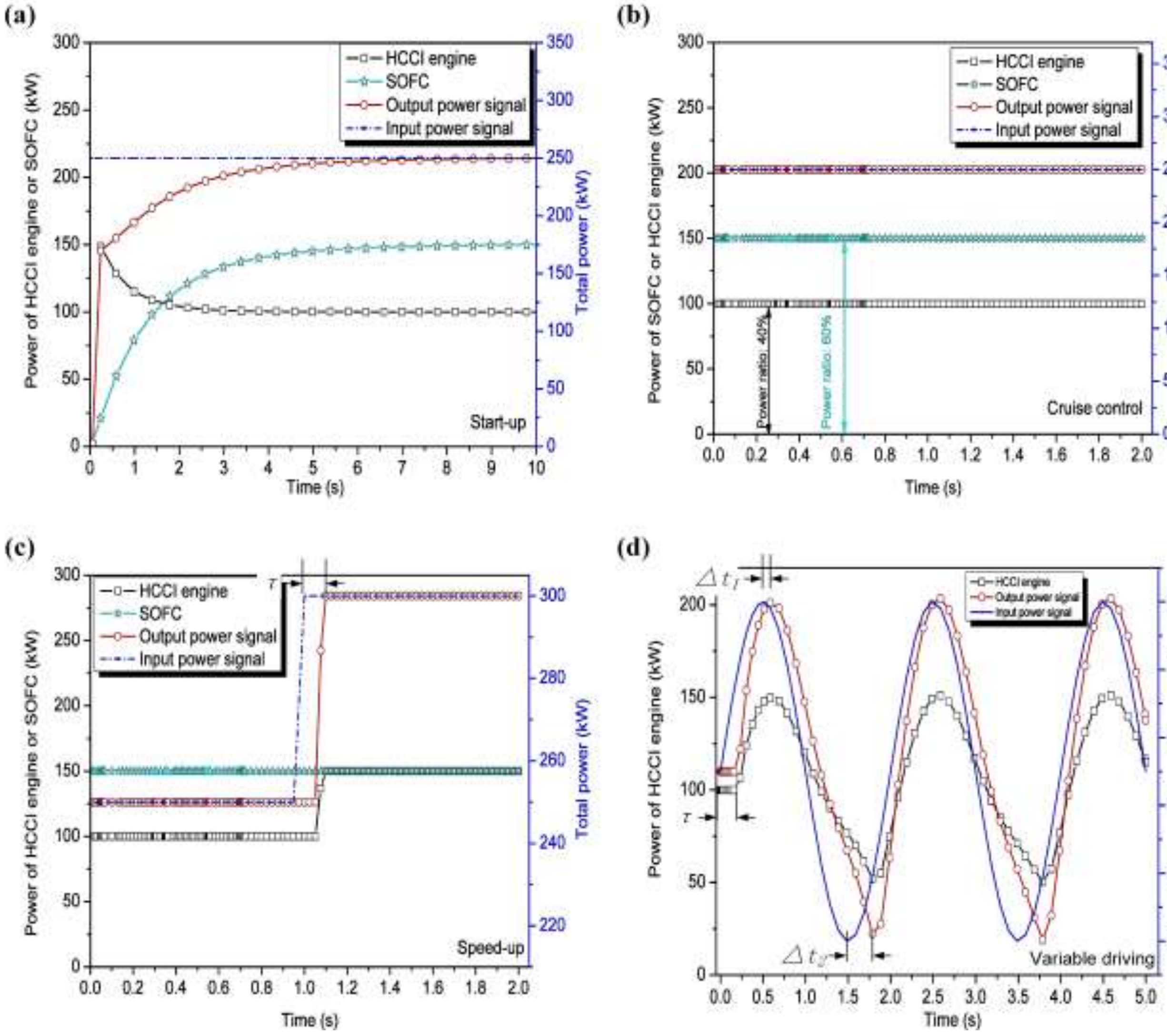

Fig. 14 Transient response of the main components and the hybrid power system at different typical driving cycles. (a) Start-up cycle; (b) Cruise control; (c) Speed-up cycle; (d) Variable driving cycle

4. Conclusions

In summary, the dynamic modeling of a novel SOFC-Engine hybrid energy conversion system with hydrogen addition by the metal hydride and waste heat recovery unit is performed in this study. This work provides an insight into the dynamic behaviors of the SOFC-Engine hybrid system for practical applications in the large mobile vehicles. Specifically, the dynamic response characteristics and operation strategy of the hybrid power system are discussed and provided. Besides, the operation strategy is further investigated for the dynamic optimization. The following conclusions can be drawn:

(1) Although the HCCI engine has faster dynamic behavior than the SOFC, its autonomy is

partly restricted by the SOFC without H_2 addition. This is because that the engine fuel directly comes from the SOFC off-gas. Therefore, the relatively slow dynamic of the SOFC dominates the system dynamic in the case without H_2 addition.

(2) To enhance the engine autonomy, the method of using waste heat recovery to drive hydrogen desorption of metal hydride for the engine is introduced into the hybrid system. The hydrogen addition by a metal hydride reactor and hydrogen tank not only enhances the dynamic behavior, but also improves the overall conversion efficiency of the hybrid system, which can be improved to 67.6% with the hydrogen addition χ=2.0.

(3) The power distribution between the SOFC and the engine plays an important role in the performance optimization of the hybrid system. An effective control strategy is proposed: the fuel utilization is used to regulate the SOFC power according to the required power distribution, and the H_2 addition is used to regulate the remaining engine power. The moderate power distribution of 50%~60% for the SOFC facilitates the optimal overall performance for the hybrid system.

(4) Considering the SOFC with high efficiency and the engine with fast dynamics, the operation strategy that the SOFC provides most of the output power as a power baseline while the engine copes with the dynamics is suggested. In such an operation strategy, the hybrid system enables to respond to the change of power load within 1 s and simultaneously has a high overall energy conversion efficiency of 74.8%. Therefore, the proposed SOFC-Engine hybrid system with H_2 addition by metal hydride and waste heat recovery unit is a potential energy conversion system for mobile applications.

Acknowledgments

Z. Wu thanks the funding support from the National Natural Science Foundation of China (21736008), the Natural Science Foundation of Shaanxi Province (No. 2020JM-014), and Hong Kong Scholar Program (XJ2017023). P. Tan thanks the funding support from CAS Pioneer Hundred Talents Program and USTC Tang Scholar (KJ2090130001) and USTC Tang Scholar. M. Ni thanks the funding support from The Hong Kong Polytechnic University (G-YBJN and G-YW2D), a fund from RISUD (1-ZVEA), and a grant (Project Number: PolyU 152214/17E) from Research Grant Council, University Grants Committee, Hong Kong SAR.

References

[1] Zhou N, Price L, Yande D, Creyts J, Khanna N, Fridley D, et al. A roadmap for China to peak carbon dioxide emissions and achieve a 20% share of non-fossil fuels in primary energy by 2030. Appl Energy 2019;239:793–819. doi:10.1016/j.apenergy.2019.01.154.

[2] Zhong W, An H, Fang W, Gao X, Dong D. Features and evolution of international fossil fuel trade network based on value of emergy. Appl Energy 2016;165:868–77. doi:10.1016/j.apenergy.2015.12.083.

[3] Pedrozo VB, May I, Guan W, Zhao H. High efficiency ethanol-diesel dual-fuel combustion: A comparison against conventional diesel combustion from low to full engine load. Fuel 2018;230:440–51. doi:10.1016/j.fuel.2018.05.034.

[4] Saidur R, Rezaei M, Muzammil WK, Hassan MH, Paria S, Hasanuzzaman M. Technologies to recover exhaust heat from internal combustion engines. Renew Sustain Energy Rev 2012;16:5649–59. doi:10.1016/j.rser.2012.05.018.

[5] Qi Y, Espinoza-Andaluz M, Thern M, Andersson M. Polymer electrolyte fuel cell system level modelling and simulation of transient behavior. eTransportation 2019;2:100030. doi:10.1016/j.etran.2019.100030.

[6] Zhang H, Kong W, Dong F, Xu H, Chen B, Ni M. Application of cascading thermoelectric generator and cooler for waste heat recovery from solid oxide fuel cells. Energy Convers Manag 2017;148:1382–90. doi:10.1016/j.enconman.2017.06.089.

[7] Sulaiman N, Hannan MA, Mohamed A, Ker PJ, Majlan EH, Wan Daud WR. Optimization of energy management system for fuel-cell hybrid electric vehicles: Issues and recommendations. Appl Energy 2018;228:2061–79. doi:10.1016/j.apenergy.2018.07.087.

[8] Tanaka S, Nagumo K, Yamamoto M, Chiba H, Yoshida K, Okano R. Fuel cell system for Honda CLARITY fuel cell. eTransportation 2020;3:100046. doi:10.1016/j.etran.2020.100046.

[9] Ramírez-Minguela JJ, Rangel-Hernández VH, Alfaro-Ayala JA, Uribe-Ramírez AR, Mendoza-Miranda JM, Belman-Flores JM, et al. Energy and entropy study of a SOFC using

biogas from different sources considering internal reforming of methane. Int J Heat Mass Transf 2018;120:1044–54. doi:10.1016/j.ijheatmasstransfer.2017.12.111.

[10] Al-Hamed KHM, Dincer I. A new direct ammonia solid oxide fuel cell and gas turbine based integrated system for electric rail transportation. eTransportation 2019;2:100027. doi:10.1016/j.etran.2019.100027.

[11] Liu Y, Han J, You H. Performance analysis of a CCHP system based on SOFC/GT/CO2 cycle and ORC with LNG cold energy utilization. Int J Hydrogen Energy 2019;44:29700–10. doi:10.1016/j.ijhydene.2019.02.201.

[12] Sghaier SF, Khir T, Ben Brahim A. Energetic and exergetic parametric study of a SOFC-GT hybrid power plant. Int J Hydrogen Energy 2018;43:3542–54. doi:10.1016/j.ijhydene.2017.08.216.

[13] Habibollahzade A, Gholamian E, Houshfar E, Behzadi A. Multi-objective optimization of biomass-based solid oxide fuel cell integrated with Stirling engine and electrolyzer. Energy Convers Manag 2018;171:1116–33. doi:10.1016/j.enconman.2018.06.061.

[14] Hosseinpour J, Sadeghi M, Chitsaz A, Ranjbar F, Rosen MA. Exergy assessment and optimization of a cogeneration system based on a solid oxide fuel cell integrated with a Stirling engine. Energy Convers Manag 2017;143:448–58. doi:10.1016/j.enconman.2017.04.021.

[15] Vollmar H-E, Maier C-U, Nölscher C, Merklein T, Poppinger M. Innovative concepts for the coproduction of electricity and syngas with solid oxide fuel cells. J Power Sources 2000;86:90–7. doi:10.1016/S0378-7753(99)00421-8.

[16] Kang S, Ahn K-Y. Dynamic modeling of solid oxide fuel cell and engine hybrid system for distributed power generation. Appl Energy 2017;195:1086–99. doi:10.1016/j.apenergy.2017.03.077.

[17] Lee YD, Ahn KY, Morosuk T, Tsatsaronis G. Exergetic and exergoeconomic evaluation of an SOFC-Engine hybrid power generation system. Energy 2018;145:810–22. doi:10.1016/j.energy.2017.12.102.

[18] D.F. Chuahy F, Kokjohn SL. Solid oxide fuel cell and advanced combustion engine combined cycle: A pathway to 70% electrical efficiency. Appl Energy 2019;235:391–408.

doi:10.1016/j.apenergy.2018.10.132.

[19] Oh S, Song HH. Exergy analysis on non-catalyzed partial oxidation reforming using homogeneous charge compression ignition engine in a solid oxide fuel cell system. Int J Hydrogen Energy 2018;43:2943–60. doi:10.1016/j.ijhydene.2017.12.090.

[20] Choi W, Kim J, Kim Y, Kim S, Oh S, Song HH. Experimental study of homogeneous charge compression ignition engine operation fuelled by emulated solid oxide fuel cell anode off-gas. Appl Energy 2018;229:42–62. doi:10.1016/j.apenergy.2018.07.086.

[21] Park SH, Lee YD, Ahn KY. Performance analysis of an SOFC/HCCI engine hybrid system: System simulation and thermo-economic comparison. Int J Hydrogen Energy 2014;39:1799–810. doi:10.1016/j.ijhydene.2013.10.171.

[22] Choi W, Kim J, Kim Y, Song HH. Solid oxide fuel cell operation in a solid oxide fuel cell–internal combustion engine hybrid system and the design point performance of the hybrid system. Appl Energy 2019;254:113681. doi:10.1016/j.apenergy.2019.113681.

[23] Kim J, Kim Y, Choi W, Ahn KY, Song HH. Analysis on the operating performance of 5-kW class solid oxide fuel cell-internal combustion engine hybrid system using spark-assisted ignition. Appl Energy 2020;260:114231. doi:10.1016/j.apenergy.2019.114231.

[24] Wu Z, Tan P, Zhu P, Cai W, Chen B, Yang F, et al. Performance analysis of a novel SOFC-HCCI engine hybrid system coupled with metal hydride reactor for H2 addition by waste heat recovery. Energy Convers Manag 2019;191:119–31. doi:10.1016/j.enconman.2019.04.016.

[25] Wick M, Bedei J, Gordon D, Wouters C, Lehrheuer B, Nuss E, et al. In-cycle control for stabilization of homogeneous charge compression ignition combustion using direct water injection. Appl Energy 2019;240:1061–74. doi:10.1016/j.apenergy.2019.01.086.

[26] Hagos FY, A. Aziz AR, Sulaiman SA, Mamat R. Engine speed and air-fuel ratio effect on the combustion of methane augmented hydrogen rich syngas in DI SI engine. Int J Hydrogen Energy 2019;44:477–86. doi:10.1016/j.ijhydene.2018.02.093.

[27] Al-Hamed KHM, Dincer I. A new direct ammonia solid oxide fuel cell and gas turbine based integrated system for electric rail transportation. eTransportation 2019;2:100027. doi:10.1016/j.etran.2019.100027.

[28] Chen Y, Wang M, Liso V, Samsatli S, Samsatli NJ, Jing R, et al. Parametric analysis and optimization for exergoeconomic performance of a combined system based on solid oxide fuel cell-gas turbine and supercritical carbon dioxide Brayton cycle. Energy Convers Manag 2019;186:66–81. doi:10.1016/j.enconman.2019.02.036.

[29] Li Y, Ye S, Wang W. Performance analysis of SOFC system based on natural gas autothermal reforming. CIESC J 2016;67:1557–64. doi:10.11949/j.issn.0438-1157.20150381.

[30] Burbank W, Witmer DD, Holcomb F. Model of a novel pressurized solid oxide fuel cell gas turbine hybrid engine. J Power Sources 2009;193:656–64. doi:10.1016/j.jpowsour.2009.04.004.

[31] Wu Z, Yang F, Zhang Z, Bao Z. Magnesium based metal hydride reactor incorporating helical coil heat exchanger: Simulation study and optimal design. Appl Energy 2014;130:712–22. doi:10.1016/j.apenergy.2013.12.071.

[32] Burbank W, Witmer DD, Holcomb F. Model of a novel pressurized solid oxide fuel cell gas turbine hybrid engine. J Power Sources 2009;193:656–64. doi:10.1016/j.jpowsour.2009.04.004.

[33] Stiller C, Thorud B, Seljebø S, Mathisen Ø, Karoliussen H, Bolland O. Finite-volume modeling and hybrid-cycle performance of planar and tubular solid oxide fuel cells. J Power Sources 2005;141:227–40. doi:10.1016/j.jpowsour.2004.09.019.

[34] Sedghisigarchi K, Feliachi A. Dynamic and Transient Analysis of Power Distribution Systems With Fuel Cells—Part I: Fuel-Cell Dynamic Model. IEEE Trans Energy Convers 2004;19:423–8. doi:10.1109/TEC.2004.827039.

[35] Chung CA, Ho C-J. Thermal–fluid behavior of the hydriding and dehydriding processes in a metal hydride hydrogen storage canister. Int J Hydrogen Energy 2009;34:4351–64. doi:10.1016/j.ijhydene.2009.03.028.

[36] Cheddie DF. Integration of A Solid Oxide Fuel Cell into A 10 MW Gas Turbine Power Plant. Energies 2010;3:754–69. doi:10.3390/en3040754.

[37] Correa JM, Farret FA, Canha LN, Simoes MG. An Electrochemical-Based Fuel-Cell Model Suitable for Electrical Engineering Automation Approach. IEEE Trans Ind Electron 2004;51:1103–12. doi:10.1109/TIE.2004.834972.

[38] Ni M, Leung MKH, Leung DYC. Parametric study of solid oxide fuel cell performance. Energy Convers Manag 2007;48:1525–35. doi:10.1016/j.enconman.2006.11.016.

[39] Jurado F, Valverde M, Cano A. Effect of a SOFC plant on distribution system stability. J Power Sources 2004;129:170–9. doi:10.1016/j.jpowsour.2003.11.001.

[40] RM K, B K. Design and implementation of models for analyzing the dynamic performance of distributed generators in the micro grid part Ⅰ: Micro turbine and solid oxide fuel cell. Trans D Comput Sci Eng Electr Eng 2010;17:47–58.

[41] Li YH, Choi SS, Rajakaruna S. An Analysis of the Control and Operation of a Solid Oxide Fuel-Cell Power Plant in an Isolated System. IEEE Trans Energy Convers 2005;20:381–7. doi:10.1109/TEC.2005.847998.

[42] Djermouni M, Ouadha A. Thermodynamic analysis of an HCCI engine based system running on natural gas. Energy Convers Manag 2014;88:723–31. doi:10.1016/j.enconman.2014.09.033.

[43] Osborne RJ, Li G, Sapsford SM, Stokes J LT. Evaluation of HCCI for future gasoline powertrains. SAE 2003 world Congr. Exhib., 2003.

[44] Livengood JC, Wu PC. Correlation of autoignition phenomena in internal combustion engines and rapid compression machines. Symp Combust 1955;5:347–56. doi:10.1016/S0082-0784(55)80047-1.

[45] Walton SM, He X, Zigler BT, Wooldridge MS. An experimental investigation of the ignition properties of hydrogen and carbon monoxide mixtures for syngas turbine applications. Proc Combust Inst 2007;31:3147–54. doi:10.1016/j.proci.2006.08.059.

[46] Kumar KV, Porkodi K, Rocha F. Langmuir–Hinshelwood kinetics – A theoretical study. Catal Commun 2008;9:82–4. doi:10.1016/j.catcom.2007.05.019.

[47] Massardo AF, Lubelli F. Internal Reforming Solid Oxide Fuel Cell-Gas Turbine Combined Cycles (IRSOFC-GT): Part A—Cell Model and Cycle Thermodynamic Analysis. J Eng Gas Turbines Power 2000;122:27–35. doi:10.1115/1.483187.

[48] Xu J, Froment GF. Methane steam reforming, methanation and water-gas shift: I. Intrinsic kinetics. AIChE J 1989;35:88–96. doi:10.1002/aic.690350109.

[49] Lee S, Bae J, Lim S, Park J. Improved configuration of supported nickel catalysts in a steam

reformer for effective hydrogen production from methane. J Power Sources 2008;180:506–15. doi:10.1016/j.jpowsour.2008.01.081.

[50] Chan SH, Ho HK, Tian Y. Modelling of simple hybrid solid oxide fuel cell and gas turbine power plant. J Power Sources 2002;109:111–20. doi:10.1016/S0378-7753(02)00051-4.

[51] Padullés J, Ault G., McDonald J. An integrated SOFC plant dynamic model for power systems simulation. J Power Sources 2000;86:495–500. doi:10.1016/S0378-7753(99)00430-9.

[52] Chan S., Khor K., Xia Z. A complete polarization model of a solid oxide fuel cell and its sensitivity to the change of cell component thickness. J Power Sources 2001;93:130–40. doi:10.1016/S0378-7753(00)00556-5.

[53] ZHAO F, VIRKAR A. Dependence of polarization in anode-supported solid oxide fuel cells on various cell parameters. J Power Sources 2005;141:79–95. doi:10.1016/j.jpowsour.2004.08.057.

[54] Liu X, Kokjohn S, Li Y, Wang H, Li H, Yao M. A numerical investigation of the combustion kinetics of reactivity controlled compression ignition (RCCI) combustion in an optical engine. Fuel 2019;241:753–66. doi:10.1016/j.fuel.2018.12.068.

[55] Nerat M. Modeling and analysis of short-period transient response of a single, planar, anode supported, solid oxide fuel cell during load variations. Energy 2017;138:728–38. doi:10.1016/j.energy.2017.07.133.

[56] Tarasov BP, Bocharnikov MS, Yanenko YB, Fursikov P V., Lototskyy M V. Cycling stability of RNi5 (R = La, La+Ce) hydrides during the operation of metal hydride hydrogen compressor. Int J Hydrogen Energy 2018;43:4415–27. doi:10.1016/j.ijhydene.2018.01.086.

[57] Fuel Cell Technologies Office. Multi-Year Research, Development, and Demonstration Plan – Part 3.3 Hydrogen Storage. 2015. doi:https://www.energy.gov/sites/prod/files/2015/05/f22/fcto_myrdd_storage.pdf.

[58] Kyoung S, Ferekh S, Gwak G, Jo A, Ju H. Three-dimensional modeling and simulation of hydrogen desorption in metal hydride hydrogen storage vessels. Int J Hydrogen Energy 2015;40:14322–30. doi:10.1016/j.ijhydene.2015.03.114.

[59] Jensen JO, Vestbø AP, Li Q, Bjerrum NJ. The energy efficiency of onboard hydrogen storage. J Alloys Compd 2007;446–447:723–8. doi:10.1016/j.jallcom.2007.04.051.

[60] Chibani A, Bougriou C, Merouani S. Simulation of hydrogen absorption/desorption on metal hydride LaNi5-H2: Mass and heat transfer. Appl Therm Eng 2018;142:110–7. doi:10.1016/j.applthermaleng.2018.06.078.

[61] Wang D, Wang Y, Huang Z, Yang F, Wu Z, Zheng L, et al. Design optimization and sensitivity analysis of the radiation mini-channel metal hydride reactor. Energy 2019;173:443–56. doi:10.1016/j.energy.2019.02.033.

[62] Jemni A. Experimental and theoretical study of ametal–hydrogen reactor. Int J Hydrogen Energy 1999;24:631–44. doi:10.1016/S0360-3199(98)00117-7.

[63] Bao Z, Yang F, Wu Z, Nyallang Nyamsi S, Zhang Z. Optimal design of metal hydride reactors based on CFD–Taguchi combined method. Energy Convers Manag 2013;65:322–30. doi:10.1016/j.enconman.2012.07.027.

[64] Sandrock G TG. IEA/DOE/SNL Hydride Databases 2010. doi:http://hydpark.ca.sandia.gov.

[65] Pang Y, Li Q. A review on kinetic models and corresponding analysis methods for hydrogen storage materials. Int J Hydrogen Energy 2016;41:18072–87. doi:10.1016/j.ijhydene.2016.08.018.

[66] Pijolat M, Favergeon L. Kinetics and Mechanisms of Solid-Gas Reactions. Handb. Therm. Anal. Calorim., 2018, p. 173–212. doi:10.1016/B978-0-444-64062-8.00011-5.

[67] Chitsaz A, Mehr AS, Mahmoudi SMS. Exergoeconomic analysis of a trigeneration system driven by a solid oxide fuel cell. Energy Convers Manag 2015;106:921–31. doi:10.1016/j.enconman.2015.10.009.

[68] Chan S., Low C., Ding O. Energy and exergy analysis of simple solid-oxide fuel-cell power systems. J Power Sources 2002;103:188–200. doi:10.1016/S0378-7753(01)00842-4.

[69] Owebor K, Oko COC, Diemuodeke EO, Ogorure OJ. Thermo-environmental and economic analysis of an integrated municipal waste-to-energy solid oxide fuel cell, gas-, steam-, organic fluid- and absorption refrigeration cycle thermal power plants. Appl Energy 2019;239:1385–401. doi:10.1016/j.apenergy.2019.02.032.

[70] Feng P, Liu Y, Ayub I, Wu Z, Yang F, Zhang Z. Techno-economic analysis of screening metal hydride pairs for a 910 MWhth thermal energy storage system. Appl Energy 2019;242:148–56. doi:10.1016/j.apenergy.2019.03.046.

[71] Zhang F, Grigoriadis KM, Franchek MA, Makki IH. Linear Parameter-Varying Lean Burn Air-Fuel Ratio Control for a Spark Ignition Engine. J Dyn Syst Meas Control 2007;129:404–14. doi:10.1115/1.2745849.

[72] Dicks AL, Fellows RG, Martin Mescal C, Seymour C. A study of SOFC–PEM hybrid systems. J Power Sources 2000;86:501–6. doi:10.1016/S0378-7753(99)00492-9.